A new framework to incorporate high-latitude input for meso-scale electrodynamics: HIME

D. S. Ozturk[1], X. Meng[1], O. P. Verkhoglyadova[1], R. H. Varney[2], A. S. Reimer[2], J. L. Semeter[3]

[1]Jet Propulsion Laboratory, California Institute of Technology, Pasadena, California, USA
[2]Center for Geospace Studies, SRI International, Menlo Park, CA, USA
[3]Center for Space Physics, Boston University, Boston, MA, USA

Key Points:

- For the first time local, dynamic, 2D electric field estimates are merged with a global empirical model.
- Local meso-scale electric field variability is successfully communicated to GITM.
- The energy deposited locally in HIME-driven simulations are higher compared to Weimer-driven simulations.

Corresponding author: Dogacan Su Ozturk, dogacan.s.ozturk@jpl.nasa.gov

Abstract

Global Circulation Models (GCMs) for the ionosphere-thermosphere system (I-T) traditionally use empirical models to specify upper boundary conditions to represent solar wind and magnetospheric drivers. However, the magnetosphere, ionosphere and thermosphere systems are coupled on different spatial and temporal scales. During increased levels of geomagnetic activity, these empirical models can't resolve dynamic electric field variability (<500 km, <15 minutes) because of their statistical nature and/or low spatial and temporal resolutions. This results in an underestimation of energy input to the ionosphere, causing disagreements between model results and observations. This paper introduces a new framework to incorporate dynamic electric fields into GCMs: High-latitude Input for Meso-scale Electrodynamics (HIME). As a demonstration HIME uses the Poker Flat Incoherent Scatter Radar (PFISR) electric field estimates during an experiment on 2 March 2017. The electric potentials were calculated using the PFISR estimates and merged with a global empirical model of electric potential. A set of high-latitude electric potential drivers were used to drive the University of Michigan Global Ionosphere Thermosphere Model (GITM) to understand the effects of driving at different scales. Data vs model comparisons for ion temperature, electron temperature, and electron density are provided along the PFISR beams. The ion convection velocities and neutral winds at the PFISR location are compared with the PFISR and Scanning Doppler Imager (SDI) data. The effects of different multi-scale drivers are investigated. The results showed energy deposited by HIME-driven simulations was locally larger by approximately an order of magnitude compared to the empirical model-driven results.

1 Introduction

Magnetospheric energy is deposited to the high-latitude ionosphere mainly through Joule heating and particle precipitation processes (Knipp et al., 2004, 2005; Turner et al., 2009; Schunk & Nagy, 2009). Especially during geomagnetic storms the amount of electromagnetic energy deposited can reach up to 10^{11} W (Rodger et al., 2001). Such energy input significantly alters the I-T conditions by driving from above, generating acoustic-gravity waves (Williams et al., 1988; Balthazor et al., 1997), causing changes in wind patterns (Emery et al., 1999), density and temperature profiles (Mikhailov & Foster, 1997; Lei et al., 2004; Richards et al., 2010; Sydorenko et al., 2015). Therefore, it is necessary to realistically determine the characteristics of the energy input to understand I-T dynamics.

The dissipation of the magnetospheric energy though Joule heating can be quantified using Pedersen conductivity, electric fields, neutral winds and geomagnetic field (Schunk & Nagy, 2009). Unfortunately, as explained by Thayer (1998) the simultaneous observation of these four quantities over the entire high-latitude ionosphere is not possible. Thus, the efforts to understand IT responses to magnetospheric drivers rely mostly on global circulation models (GCMs). GCMs use empirical relations to estimate the electric field potentials (Heelis et al., 1982), (Heppner & Maynard, 1987; Iijima & Potemra, 1976; Weimer, 2005), and particle precipitation (Hardy et al., 1985; Roble & Ridley, 1987; Fuller-Rowell & Evans, 92; Newell et al., 2002; Y. Zhang & Paxton, 2008; Newell et al., 2009), which result in spatially binned and statistically averaged inputs. However, as first shown by Codrescu et al. (1995) the energy deposition can be significantly underestimated when the temporal and spatial variability of the high-latitude electric fields are ignored. Richmond (2010) argued that energy dissipated through large-scale structures (>15 minutes and >1000 km) do not make a large contribution as smaller-scale structures do over a localized region. Similarly, Brekke and Kamide (1996) demonstrated that the fluctuating electric fields can dominate the Joule heating rates by affecting the ion neutral interactions at auroral electrojet locations. The temporal and spatial distributions of the electric field fluctuations at the ionosphere were studied extensively by Cousins and Shepherd (2012), using Super Dual Auroral Radar Network (SuperDARN) radars. They have demonstrated that structures with 45 to 450 km of spatial and 2 to 20 minutes of temporal resolution exhibited changes in magnitude between ±60mV/m in magnitude. In addition, they have discussed the effects of spatial variability on temporal fluctuations and estimated the range for temporal variability to be between 10 to 16 minutes for the nightside, high-latitude ionosphere. The small- and meso-scale fluctuations defined by such studies were not resolved by the empirical models of high-latitude electric fields, contributing to the systematic underestimation of Joule heating in GCMs (Deng & Ridley, 2007; Deng et al., 2009). In general, spatiotemporal properties of high-latitude drivers are categorized through Field-Aligned Current systems (FACs), however there is no widely accepted categorization for electric field properties. Using Space Technology 5 spacecraft data, Gjerloev et al. (2011) identified the large-scale as above 200 km for FACs. Forsyth et al. (2017) used Swarm Mission current measurements and expanded the large-scale definition as above 450 km, citing the limited capabilities of single-spacecraft techniques. They also commented that the highest correlation among the spatial and temporal properties were observed above 60 seconds for large-scale currents. In this paper, we define meso-scale electric field variability as between 100 to 500 km spatially following the definition in Q. Zhu et al. (2019), and between 2-15 minutes temporally based on the Forsyth et al. (2017) study for the lower limit, and Cousins and Shepherd (2012) for the upper limit.

Data assimilation models can also be used to incorporate high-latitude drivers to GCMs. A frequently used technique is the Assimilative Mapping of Ionospheric Electrodynamics (AMIE) procedure by the National Center for Atmospheric Research (NCAR) (Richmond & Kamide, 1988; Lu et al., 2001). AMIE uses a combination of spacecraft and ground-based measurements to obtain the optimal high-latitude ionospheric electric potentials, convection patterns, conductance profiles, auroral energy flux and characteristic energy self-consistently (Lu et al., 2014). However, the performance of the AMIE technique is closely related to the data coverage, quality and resolution. In addition AMIE uses an empirical auroral conductance model to calculate the relation between electric fields and precipitation (Richmond et al., 1998). These limitations often result in underestimation of electric field variability (Crowley & Hackert, 2001; Matsuo et al., 2003; Cosgrove et al., 2009), and consequently in lower Joule heating rates and cross-polar cap potentials (Lu et al., 2001). Verkhoglyadova et al. (2017) showed that improving driver characterization could improve energy budget calculation in GCMs.

Both empirical and data assimilation models ignore the neutral wind dynamics, which is another contributing factor to Joule heating. Heelis and Coley (1988) found that there was a mismatch between the peaks of measured ion temperatures and calculated Joule heating rates when neutral winds were neglected. Thayer et al. (1995) and Thayer and Semeter (2004) theoretically showed that 10 to 30% of the electromagnetic energy was transferred to the neutrals as mechanical energy. In addition, neutrals were able to act as a dynamo generating electric fields. After the realization of the role of neutral winds, GCMs that incorporate neutral dynamics became an integral part of studies quantifying storm time energy input to the I-T system. Crowley et al. (2006) used NCAR's TIEGCM to study the 20 November 2003 magnetic storm and reported neutral wind driven composition changes from high to mid-latitude regions both in modeled response and Global Ultraviolet Imager observations. Deng and Ridley (2006) used GITM to understand the coupling between ion convection patterns and neutral winds and validated the model results with WINDII observations. Recently, J. Zhu et al. (2016) revisited the ion and electron temperature calculations in GITM, adding time-dependent energy equations, field-aligned thermal conduction, heating and cooling rates that consequently improved comparisons of GITM results to ISR measurements and the International Reference Ionosphere.

The magnetospheric magnetohydrodynamic models can provide global and high-resolution ionospheric electrodynamics input. In these models the ionospheric electric potentials can be calculated from the closure of FACs (Ahn et al., 1983; Goodman, 1995), whereas the auroral precipitation and conductance are obtained by using empirical and physical relations (Knight, 1973; Robinson et al., 1987; Janhunen et al., 1996; Raeder et al., 1998;

Ridley et al., 2004; Wiltberger et al., 2009; Khazanov et al., 2017). Many studies demonstrated that the global MHD models reproduce observed transient perturbations that link magnetosphere-ionosphere systems ((Fujita et al., 2003a; Kataoka et al., 2004; X. Y. Zhang et al., 2010; Yu. & Ridley, 2011; Ozturk et al., 2018, 2019). However, the modeled transient perturbations are mostly in the Pc-5 range with spatial scales of a few Earth radii in the magnetosphere.Furthermore, these first-principles models can not fully capture the kinetic processes associated with magnetic reconnection ((Birn et al., 2001) and references therein), and wave-particle interactions in the equatorial magnetosphere (Wiltberger et al., 2005; Connor et al., 2016). Combined with the simplifications used for auroral processes,MHD models often tend to mischaracterize the Region-2 FAC systems and precipitation patterns.

With funding from the National Science Foundation (NSF), SRI has deployed and been operating the Poker Flat Incoherent Scatter Radar (PFISR) since 2007. Line-of-sight measurements from PFISR multi-beam experiments are routinely used to construct two dimensional plasma flow and electric fields (Heinselman & Nicolls, 2008; Nicolls et al., 2014; Clayton et al., 2019). In addition PFISR provides electron density, and electron and ion temperature profiles measured along the beams.These measurements can be used to drive, regional (Grubbs et al., 2017), or validate global, numerical models (Liuzzo et al., 2014; Ozturk et al., 2018). PFISR can also run special modes on request that sample different regions or provide different resolutions. One such mode is called ”isinglass v3.0” which was designed to aid the ISINGLASS (Ionospheric Structuring: In Situ and ground-based Low Altitude Studies) mission (NASA 36.303/4, PI Kristina Lynch/Dartmouth College). ISINGLASS consisted of two sounding rockets launched into the auroral form to simultaneously measure the plasma flow field at different locations. Various ground-based sensors located in Alaska were also assisting the ISINGLASS measurements during the mission.These sensors consisted of multiple wide angle and limited field of view cameras and Fabry-Perot interferometers (Clayton et al., 2019). Using PFISR data collected during ISINGLASS, it was possible to reconstruct the F region plasma flow with a latitudinal step size of 0.25 degree spatial resolution and a temporal resolution of 66 seconds. These resolutions are sufficient to resolve meso-scale structures and the measurements display significant electric field variability both spatially and temporally.

To investigate driving by meso-scale electric fields on the I-T system, we developed a new framework, High-latitude Input for Meso-scale Electrodynamics: HIME. With this new framework we can now account for the local meso-scale electric field variability in a global I-T model, so that its role during certain intervals and locations can be analyzed. We used aforementioned local 2D electric field estimates from PFISR, calculated the electric potentials and merged them with a global empirical model to specify upper boundary conditions for GITM. With HIME-driven GITM simulations, we aim to analyze the energy transferred to the I-T system through the meso-scale electric fields and determine the fundamental physical processes that cause the observed and simulated localized changes in plasma parameters. With PFISR operating continuously since March 2007, there exists more than a solar cycle of continuous ISR observations that can be used in support of global data assimilation and global model refinement efforts. Continuous ISR observations also present an opportunity for use in nowcasting. Thus it is timely and crucial to develop such a framework that can incorporate meso-scale driving in global models to further understand the dynamics and energy budget of the high-latitude IT system at multi-scale.

This paper discusses the HIME methodology to incorporate the 2D PFISR electric field vector estimates derived from the special ’isinglassv3.0’ mode during 2 March 2017. The data sets used for driving and validating the model are described in the next section. The adaptation of upper boundary conditions to incorporate localized 2D electric fields is detailed in Section 2.2. Section 3 discusses the modelvalidation with PFISR line of sight measurements and Scanning Doppler Imager (SDI) data. In Section 4, we examine the implications of data-model comparisons and differences in underlying physical mechanisms between large- and meso-scale driving. This is followed by a discussion on sources of uncertainties, and possible future directions to improve the suggested HIME framework. We conclude with the summary and key findings of the study in the last section.

2 Methodology

2.1 Data Sets

2.1.1 Solar wind and IMF Conditions on 2 March, 2017

The 1 minute averages of IMF (a), solar wind velocity (b), density (c), dynamic pressure (d), symH index (e) and AE (f) data from the OMNI database (https://omniweb.gsfc .nasa.gov/form/omni min.html) are presented in Figure 1. The storm onset was around 0430 UT on 1 March. The solar wind speed gradually increased from 400 km/s to 700 km/s over the course of 20 hours as shown in Figure 1b.The solar wind density shown in Figure 1c also increased in the first 8 hours of this period, then started decreasing around 1200 UT on 1 March. Figure 1d shows the solar wind dynamic pressure, which follows a similar trend to solar wind density, however the decrease following 1200 UT was not as sharp due to the drop in solar wind velocity. The symH index presented in Figure 1e showed a gradual drop following the storm onset. In addition, the AE index in Figure 1f showed an initial short-lived elevation around 0600 UT on 1 March, followed by a series of stronger enhancements starting around 1000 UT.

The interval selected for study coincides with the the recovery phase of the storm, between 0630 UT to 0800 UT (blue shaded region) on 2 March. The IMF B_Z had multiple turnings at this interval, but mostly stayed negative between 0648 UT-0732 UT. The solar wind speed was around 650 km/s indicating high speed streams.The variations in solar wind density and dynamic pressure were small during this time. The AE index was fluctuating and had two peaks at 500 nT around 0645 UT and 07220 UT on 2 March.These solar wind and IMF values were used as input for the empirical convection and precipitation models.

2.1.2 PFISR Measurements

Located at the Poker Flat Research Range (65.13° N and 147.57° W in geographic and 65.4° N and 93.5° W in magnetic coordinates), PFISR is a phased-array radar, which can be steered on a pulse-to-pulse basis (Heinselman & Nicolls, 2008). The steering allows for different beam measurements to be combined into a simultaneous measurement when integrated over time (J. Semeter et al., 2010; Nicolls et al., 2014).

This study uses the technique introduced by Nicolls et al. (2014) to estimate the F-region electric potential on a 2-D grid from the PFISR line-of-sight velocity measurements. The technique determines F-region electric potential that is consistent with the PFISR line-of-sight velocities assuming F-region velocities are dominated by the $E \times B$ drift and has the smoothest electric fields. The formulation in terms of electric potential guarantees the resulting electric field estimate is curl-free. For a monostatic radar with a modest number of beam positions the inverse problem is ill-posed and underdetermined. The problem is regularized by minimizing a measure of the roughness of the electric fields while constraining the solution with the line-of-sight measurements.

The PFISR operation mode was '*isinglass*v3.0' which took place between 0626 UT to 1700 UT (2226 to 0900 local time) on March 2, 2017 to support the ISINGLASS sounding rocket experiment (Clayton et al., 2019). This experiment was designed to provide high cadence F-region measurements under the expected trajectory of the ISINGLASS sounding rocket. All pulses are 330μs uncoded long pulses which are then input into autocorrelation functions and fit at 24.5 km range resolution. The experiment interleaves three frequency channels and 15 beam positions pointed downrange, with the 10 beam positions in the center under the expected rocket trajectory being revisited three times as frequently as the 5 beams on the edges. The beam configurations are shown in Figure 2a (geo) and b

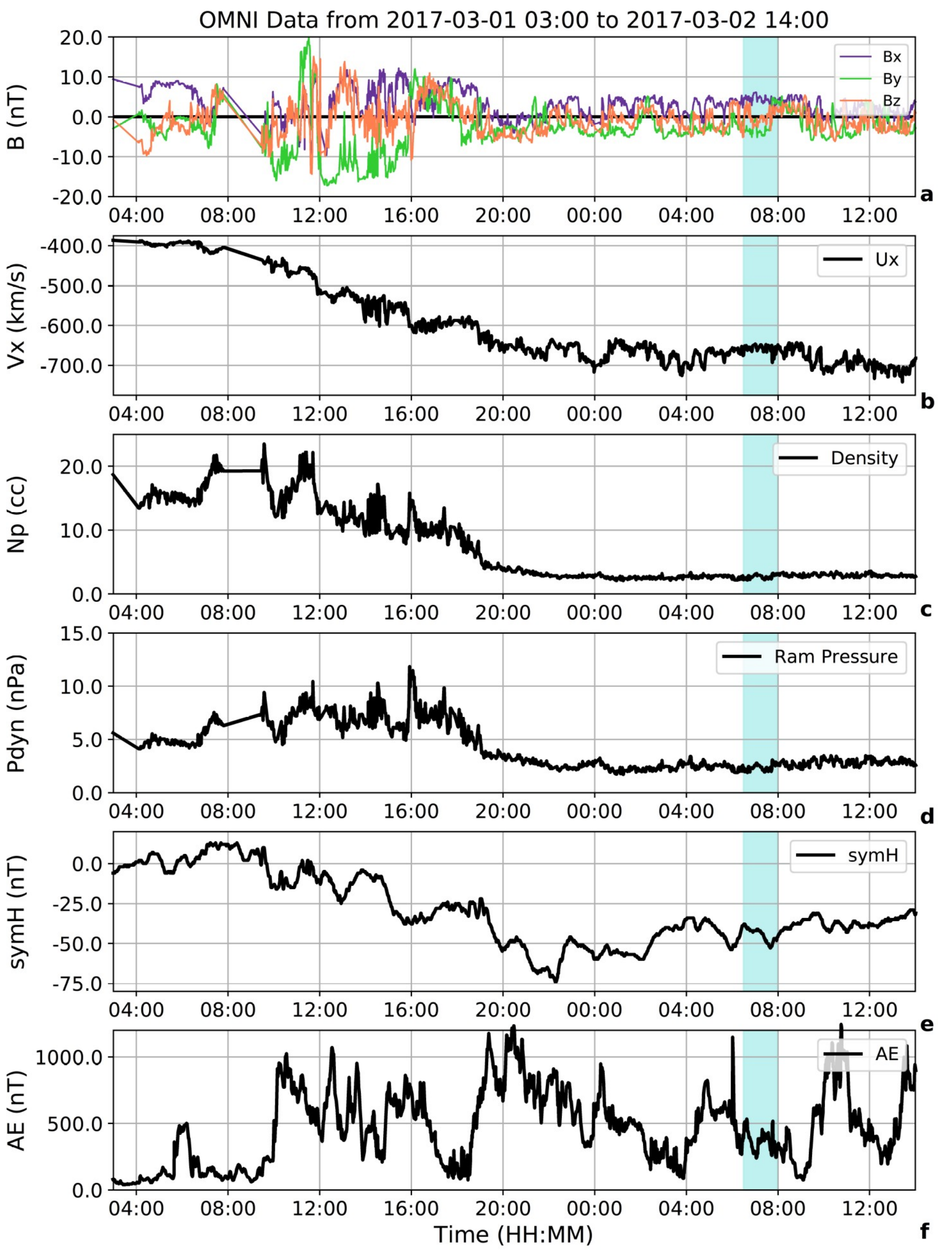

Figure 1. The OMNI values of x (purple), y (green), z (orange) components of magnetic field (a), the x component of solar wind velocity (b), solar wind density (c), dynamic pressure (d) and symH index (e) are shown between 1 March 2017 0300 UT to 2 March 2017 1400 UT. The blue shaded region between 0630-0800 UT shows the time interval studied with PFISR driven electric fields.

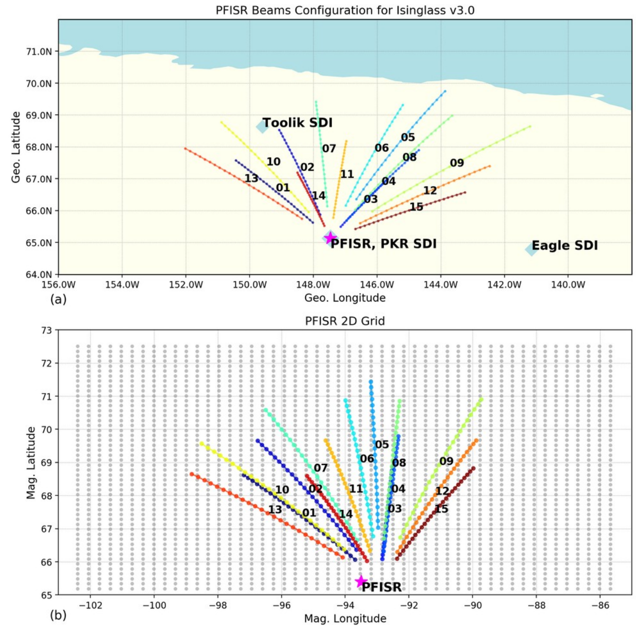

Figure 2. The PFISR beam configurations shown in geographic coordinates (a) and in magnetic coordinates with the 2D grid points (b). Each beam is shown with a different color. The pink star shows the location of PFISR, the blue diamonds show the locations of SDI sites.

(mag). The pulse sequence repeats once every 0.735 s, and each sequence contains 6 or 2 pulses per frequency channel per beam in the center or edges, respectively. The fitted data presented here integrates over 90 sequences (66.15 s) and combines all frequency channels, thus providing 1620 or 540 pulses worth of statistics in the center or edges, respectively. The 2D grid for the estimated electric field values are shown in 2b. The spatial resolution of the estimated electric fields is 0.15° in magnetic latitude and 0.34° in magnetic longitude, on a 7.5° in latitude, 16.5° in longitude domain, which is larger than the area covered by the PFISR data itself.

2.1.3 Scanning Doppler Imagers

The F region neutral wind velocity vectors are obtained from three all-sky scanning Doppler imagers (SDI) located in Alaska (http://sdi_server.gi.alaska.edu/sdiweb/index.asp). The SDIs are located at the Eagle [64.78° N, 141.15° W], Poker Flat Research Range [65.12° N, 147.43° W], and Toolik [68.63° N, 149.6° W] sites and are shown with blue diamonds on Figure 2a. SDIs in these sites are wide FOV Fabry-Perot interferometers collecting optical emission profiles at different wavelengths, which are combined with the Doppler shifts to derive LOS velocities (Conde & Smith, 1995). The zonal and meridional winds were then inferred from the LOS winds ((Dhadly et al., 2015) and references therein). For this study, the 6300 Å Oxygen red line profiles corresponding to ~250 km altitude (Schunk & Nagy, 2009) were used. The temporal resolution of the data is 2.5 minutes, with Eagle site only covering the interval between 0645 UT to 0733 UT.

2.1.4 All-sky Camera Images

The visible auroral intensity between 0630-0800 UT is studied through the Poker Flat digital all-sky camera (DASC) collocated with PFISR in Alaska, 65.12° N, 147.43° W (Conde et al., 2001). DASC uses an Electron Multiplying Charge-Coupled Device and has three filters for 427.8 nm (blue), 557.7 nm (green), and 630.0 nm (red) emissions and it cycles through these filters with a temporal resolution of 12.5 seconds between consecutive sampling at the same wavelength (Fernandes et al., 2016). The Poker Flat DASC data is available through http://optics.gi.alaska.edu/optics/. In this study the green and red emission lines are used, which correspond to[c1] 100-150 km interval and 250 km altitudes respectively.

2.2 Description of HIME Framework

The default high-latitude drivers for GCMs are inherently large-scale. Therefore, the HIME framework has been developed to incorporate meso-scale drivers as high-latitude boundary conditions to drive GCMs. In this framework ISR measurements, which carry information about the local meso-scale drivers,specifically electric fields are incorporated to a global empirical model of high-latitude electric potentials. With this approach a multi-scale global potential pattern could be defined which would enable simulating similar local conditions over measurement sites. We used HIME-driven GITM simulations to further investigate the effects of meso-scale electric fields on the local I-T system.

GITM is a first-principle global ionosphere-thermosphere model developed at the University of Michigan (Ridley et al., 2006). It solves Navier-Stokes equations for neutrals and transport equations for plasmas on a three-dimensional, geographic longitude, latitude and altitude based, non-uniform, stretched grid, assuming a non-hydrostatic solution. The model self-consistently solves for the electron, ion and neutral temperatures (J. Zhu et al., 2016). The heating terms in GITM are EUV, Joule, auroral, conduction and chemical heating, whereas the cooling is calculated from NO, CO_2, and O_2 radiative cooling terms.

By default GITM uses the Weimer Model (Weimer, 2005) to specify the upper boundary conditions for the electric potentials (Ridley et al., 2006). Based on 45-minute averaged measurements from the Dynamics Explorer-2, IMP-8, and ISEE-3 satellites, the Weimer model provides electric potentials in Altitude Adjusted Corrected Geomagnetic Coordinates; binned based on solar wind, IMF parameters, and tilt angle (Weimer, 2005). To determine the auroral precipitation the Oval Variation, Assessment,Tracking, Intensity and Online Nowcasting (OVATION) model was selected from amongst the models built into GITM. The OVATION model provides the location and intensity of the auroral oval, taking into account precipitation from electron and ion diffuse aurora, in addition to the mono-energetic and broadband precipitations from discrete aurora (Newell et al., 2009). The resolution of the auroral precipitation output is 0.25h in magnetic local time, 0.25 $^\circ$ in magnetic latitude and 15 minutes in time (Newell et al., 2002).

The HIME outputs are introduced as upper boundary conditions for the electric potentials through existing AMIE framework into GITM (Yigit & Ridley, 2011; Verkhoglyadova et al., 2017) through a user defined box region. This procedure does not require a major modification to the GITM source code and only involved interfacing efforts. The calculation of the potential patterns and the grid resolution selection procedures to prepare these high-latitude boundary conditions are described in the following sections.

2.2.1 Electric Potential Calculation

At high-latitudes, the two most important drivers for the I-T system are the electric potentials and the auroral precipitation. In order to drive the global system, GITM requires electric field potentials defined at each grid point. To further investigate the effects of the meso-scale structures seen in PFISR observations, we first calculate the contribution to electric potential through these fields.

[c1] *DSO*: ~~150~~

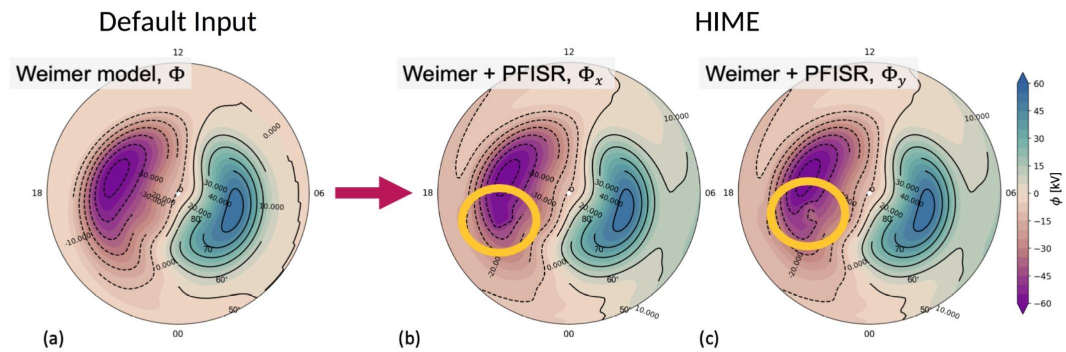

Figure 3. The electric potentials from Weimer model (a), combined with the differences calculated from PFISR measurements in x (b) and y (c) directions at 0630 UT, 02 March 2017.

The PFISR electric field measurements provide x (zonal) and y (meridional) components, which are the gradients of the electric potential in x and y directions as shown in Equation 1.

$$E_x = -\frac{\partial \Phi}{\partial x},\ E_y = -\frac{\partial \Phi}{\partial y} \tag{1}$$

Using the forward Euler method to integrate the electric fields, the x and y components of the electric potential can be found as shown in Equations 2 and 3.

$$\Delta\Phi_{x_i} = \Phi_{x_{i+1}} - \Phi_{x_i} = -E_{x,i}\ 4\,x, \tag{2}$$

$$\Delta\Phi_{y_j} = \Phi_{y_{j+1}} - \Phi_{y_j} = -E_{y,j}\ 4\,y \tag{3}$$

The potential differences, which will result in measured electric fields on the same grid once derived, can then be added to a baseline potential solution, such as Weimer potentials to drive a global numerical model. Figure 3 summarizes the difference between default input versus the HIME input. Figure 3a shows the Weimer potentials which are combined with $\Delta\Phi_x$ (b) and $\Delta\Phi_y$ (c) at 0630 UT. In order to eliminate the boundary discontinuity between the baseline and the added potentials, the built-in 2D Gaussian filter in the SciPy Library (Jones et al., 2001) was used. The 2D Gaussian filter is a convolution operator that determines the degree of smoothing based on the standard deviation of the fitted distributions.

2.2.2 Determination of the grid size

GITM currently does not have an adaptive mesh refinement implemented, however significant work is ongoing to incorporate nested grids (Deng et al., 2019). For global applications the grid size is typically chosen as 4° in longitude and 1° in latitude. The PFISR 2D electric field estimates for the isinglassv.3 mode, has a spatial resolution of 0.15° in magnetic latitude and 0.34° in magnetic longitude. In order to resolve the meso-scale electric fields, the grid size in the global domain should be smaller than the default values. However, for a global application with uniform grid sizes, the computational cost increases significantly with increased resolution. To determine the optimum grid size, the electric field estimates were first downsampled to uniform grids. Then, the electric potentials were calculated using the Forward Euler formula shown in Equations 2 and 3. Using the central differencing algorithm, which is identical to the one used in GITM, the new electric fields

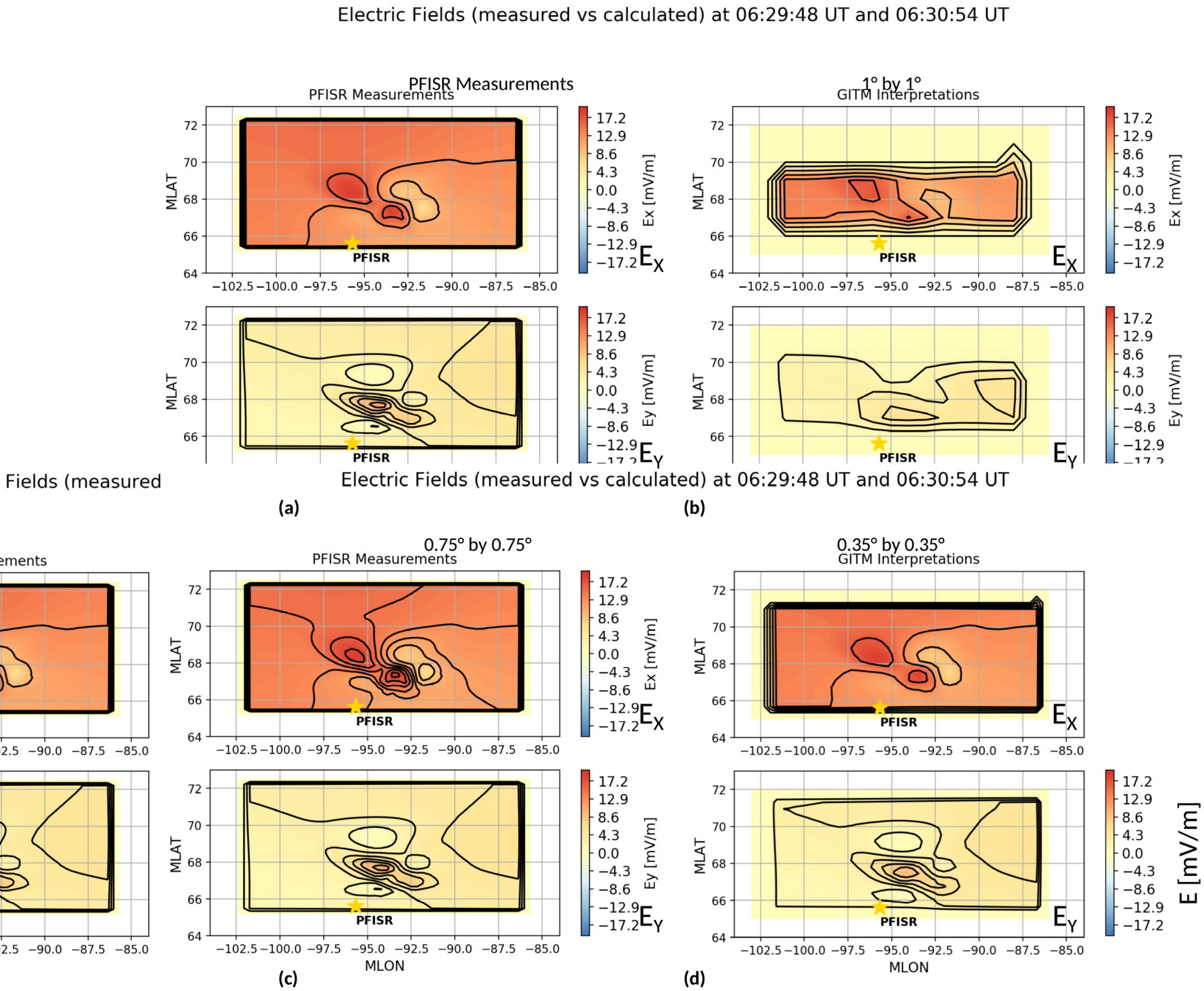

Figure 4. The contours in x (top) and y (bottom) directions at 0629 UT showing PFISR measured (a) and derived electric fields with 1° × 1° (b), 0.75° × 0.75° (c), 0.35° × 0.35° (d) sampling.[c2]

in x and y directions were calculated. [c1]Figure 4 shows x (top) and y (bottom) components of estimated PFISR electric fields (a) and down sampled electric fields on 1° × 1° (b), 0.75° × 0.75° (c), and 0.35° × 0.35° (d) grids. As the grid size decreases, more of the electric field features were resolved.

The percentage errors between the PFISR estimated and the calculated electric fields, omitting the boundaries, for different grid sizes are shown in Figure 5a and b for x and y components respectively.The boxplot shows the distribution of percentage errors averaged over the entire grid between 0630-0800 UT. The purple lines inside the boxes show the

[c1] *DSO*: ~~The PFISR 2D electric field estimates (a), and the electric fields calculated on 1° × 1° (b), 0.75° × 0.75° (c), and 0.35° × 0.35° (d) grids are shown in Figure 4 for x (top) and y (bottom) components.~~

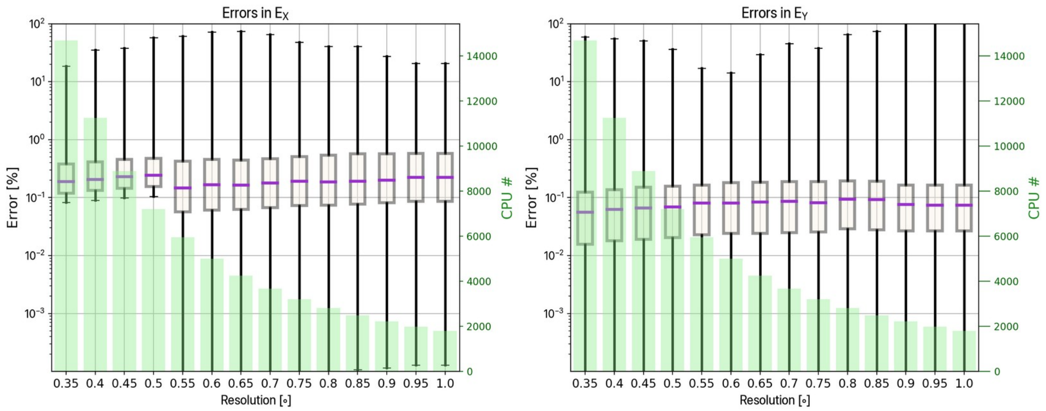

Figure 5. The electric field percentage errors for different grid resolutions calculated in x and y directions are shown. The box plots display the distribution of the mean error throughout the grid at a given time for a given resolution, purple lines show the median of error values. Green bars show the required amount of CPU nodes for each [c2] grid resolution.

median of the distribution. To find the computationally optimum grid, the CPUs needed for each operation are shown with green bars on Figure 5. [c3] The relationship between the grid resolution and required nodes is non-linear. Consequently, the computational costs increase significantly as the resolution increases, as well as the memory requirements for each run. Therefore, the 0.75° was chosen as the computationally most effective grid size to resolve meso-scale features as defined in this study. The distance between grids are around 80 km in latitude, and 35 km in longitude close to PFISR. The PFISR electric field estimates were down-sampled to a 0.75 grid to calculate the global HIME potentials.

2.2.3 Simulation Setup

The simulations were driven by 1-minute resolution OMNI solar wind and IMF data, starting from 2 days prior to the event, 28 February 2017 0600 UT, to allow for initialization. The F10.7 flux (available from the NOAA Space Weather Prediction Center, ftp://ftp.swpc.noaa.gov/pub/indices/old_indices/2017_DSD.txt)was used for ionospheric conductance calculations. The electric fields were obtained from Weimer (Weimer, 2005) and the auroral precipitation was obtained from the OVATION Model (Newell et al., 2009). The simulation grid covered the entire globe with a uniform 0.75° grid size in latitude and longitude, and the altitude extended from 100 to 600 km with a resolution of one third of the scale height. [c3]

[c4] The Weimer Model (Weimer, 2005) represents the large-scale electric fields in the ionosphere, however it can still underestimate the magnitude of these fields (Rastatter et al., 2016). Comparing the results from Weimer driven GITM simulations with the HIME-driven GITM simulations will not directly address how the meso-scale electric fields are affecting

[c3] *DSO*: ~~Based on these results, 0.75° was chosen as the computationally most effective grid size to resolve meso-scale features and the HIME potentials were calculated using 0.75° grid resolution.~~

[c3] *DSO*: ~~The PFISR electric field estimates can be decomposed into quasi-static (background, large-scale) electric fields and dynamic electric fields.~~

[c4] *DSO*: ~~Even though the Weimer Model~~ (Weimer, 2005) represents the large-scale electric fields in the ionosphere, it can still underestimate the magnitude (Rastatter et al., 2016).

the I-T system because of the difference in magnitude of the large-scale electric fields.[c5]The PFISR electric field estimates can be decomposed into quasi-static (background, large-scale) electric fields and dynamic electric fields to address this problem. [c6]To calculate the background electric fields, we take the boxcar average of the PFISR electric field estimates as shown in Equation 5.

$$E_{background_{x,i}} = < E_{x,i} >_{30min.} \quad (4)$$

$$E_{background_{y,i}} = < E_{y,i} >_{30min.} \quad (5)$$

[c1]Here $E_{x,i}$ and $E_{y,i}$ shows the x and y components of the PFISR electric field estimates. The chevron brackets, <, >, show the time averaging. The 30 minute duration was selected for the boxcar averaging since it is twice the period of the temporal upper limit of meso-scale fields. These background electric fields are then used to calculate background electric potentials, as was previously shown in Equations 2 and 3.

[c2]The dynamic electric fields can be calculated by subtracting the background electric fields from the PFISR estimates.

$$E_{variable_{x,i}} = E_{x,i} - E_{background_{x,i}} \quad (6)$$

$$E_{variable_{y,i}} = E_{y,i} - E_{background_{y,i}} \quad (7)$$

[c3]Here $E_{background_{x,i}}$ and $E_{background_{y,i}}$ are the 30-minute boxcar averages calculated for the i^{th} time step. Similarly, the variable electric potentials are calculated from these variable electric fields and combined with the Weimer Model as discussed in Section 2.2.1.

The 30 minute boxcar averaged values for the x (a) and y (d) components of the PFISR electric field estimates at 0639 UT are shown on the top row of Figure 6 to demonstrate the drivers at a given time step. The background Ex was mostly zero, whereas the background Ey was around 30 mV/m, indicating the electric fields were mostly northward at this time. The variable x (b) and y (e) components of the estimated electric fields are shown in the middle row of Figure 6. The variability seen above the PFISR location, consisted of a positive cell towards the west and a negative cell towards the east in the longitudinal direction. The variability seen in the latitudinal component was a stronger field around PFISR with a weaker cell to the north. The bottom row of Figure 6 shows the estimated x (c) and y (f) electric fields from PFISR, where both fields show properties from both the background and variable electric fields. To summarize, four different time dependent drivers were used throughout the paper which are shown in Table 1. These runs are named as Weimer, Background, Variable and Total respectively. We will refer to these runs as GITM [W], GITM-HIME [B], GITM-HIME [V] and GITM-HIME [T] in the following sections to ease tracking of the corresponding simulation results.

We start by investigating how the different electric potential input was conveyed in GITM. Figure 7 shows data-model comparisons extracted at 210° longitude, 66° latitude for the two components of electric fields between 0630-0800 UT. The PFISR estimates

---

[c5] *DSO*: *Text added.*

[c6] *DSO*: ~~In order to differentiate the effects of these two components, w~~

[c1] *DSO*: ~~We selected a 30 minute duration for the boxcar averaging since it is twice the period of the temporal upper limit of meso-scale fields. These background electric fields are then used to calculate background electric potentials, as was previously shown in Equations 2 a~~nd 3.

[c2] *DSO*: ~~Subtracting the background electric fields from the total PFISR electric field estimates results in the variable electric fields as shown in Equations 6 a~~nd 7. Similarly, the variable electric potentials are calculated from these electric fields and combined with the Weimer Model as discussed in Section 2.2.1.

[c3] *DSO*: *Text added.*

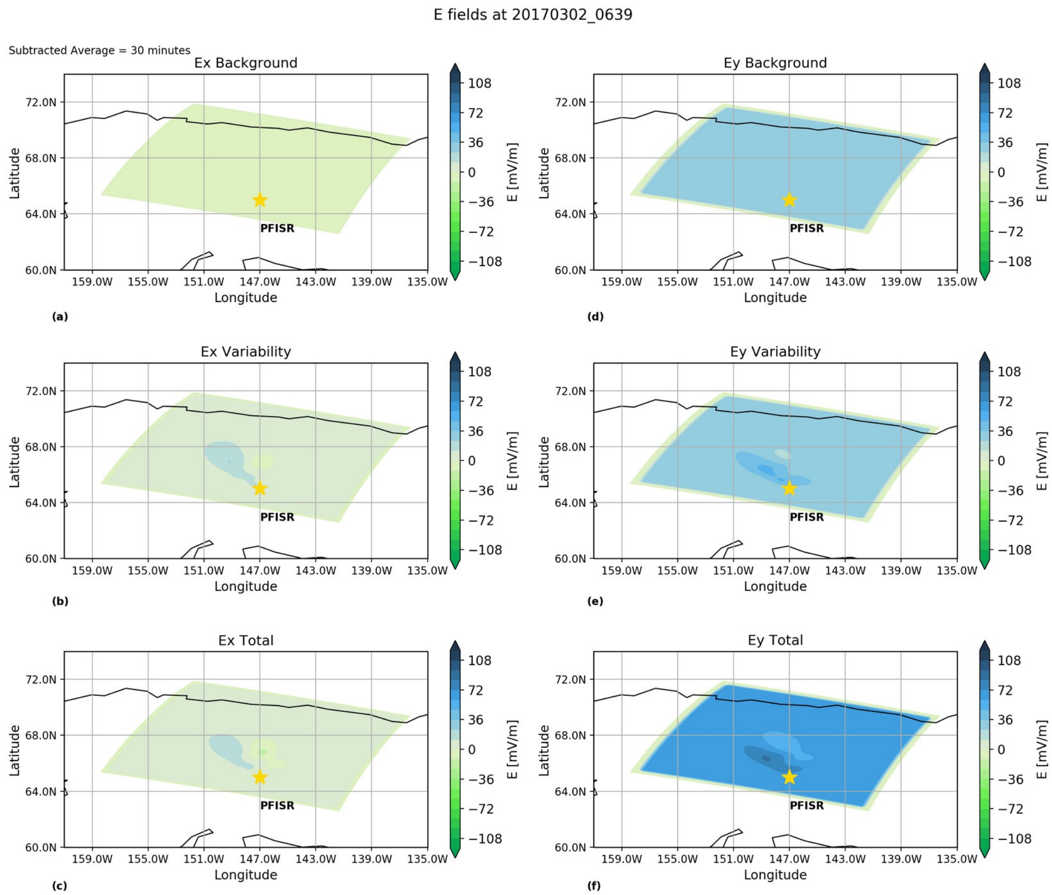

Figure 6. The background x (a), y (d), variable x (b), y (e), total x (c) and y (f) components of the 2D PFISR electric field measurements in geographic coordinates at 0639 UT. The star shows the location of PFISR.

Table 1. Definition of simulations and their drivers

Simulation Name	Potentials Used
$GITM[W]$	Weimer Model
$GITM-HIME[B]$	Weimer Model + Potentials from PFISR Background Fields
$GITM-HIME[V]$	Weimer Model + Potentials from PFISR Variable Fields
$GITM-HIME[T]$	Weimer Model + Potentials from Total PFISR Fields

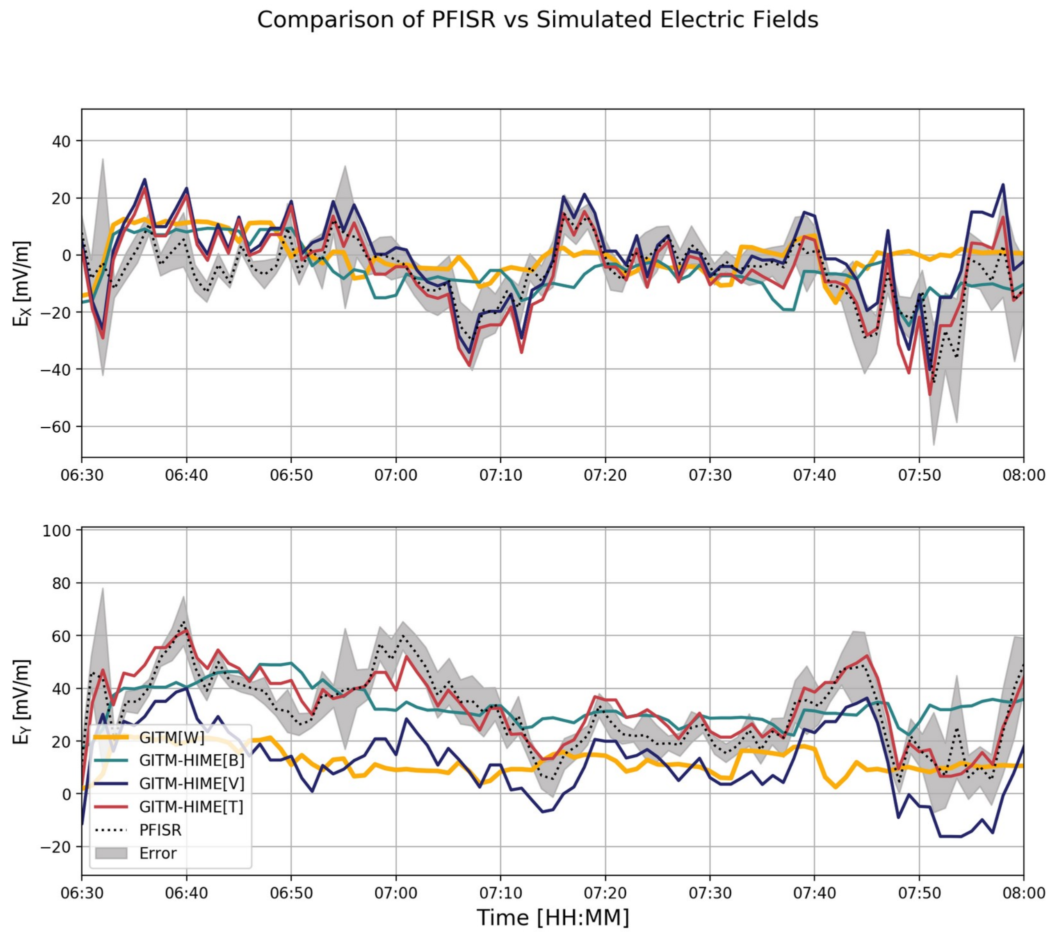

Figure 7. The temporal variation of the PFISR estimated and modeled electric field components are shown between 0630-0800 UT. The gray lines show PFISR 2D electric field estimates, the yellow (GITM[W]), green (GITM-HIME[B]), blue (GITM-HIME[V]), and red (GITM-HIME[T]) lines show simulated responses.The upper panel shows the east-west and the bottom panel shows the north-south components of electric field values taken at 210° longitude, 66° latitude.

of E_x fluctuated around 0, whereas the average values of E_y during this interval were around 30 mV/m. For both components, Background driven (GITM-HIME[B]) simulation results showed a better trend compared to estimates, as opposed to Weimer driven (GITM[W]) electric field results. Similarly, Variability driven simulation results (GITM-HIME[V]) demonstrated a more dynamic behaviour and overall a better match with the x component. Although, it was successful at capturing the timing of peaks and minimums, GITM-HIME[V] electric fields underestimated the magnitude of the electric field for the y component. For both components, Total electric field driven (GITM-HIME[T]) simulation results performed best by means of capturing both the trend and the variability seen in the PFISR estimates.

For the purpose of analyzing the results of HIME-driven GITM simulations, the quality of the fitting was examined first. The reduced χ^2 values determine the goodness of the fit, and are used in order to assess how well the data is represented by the autocorrelation functions (ACF) (Press et al., 2007). For ACFs with small errors, the reduced χ^2 values are close to 1. Here, we categorized the reduced χ^2 values as Overfit (< 0.1), Good fit

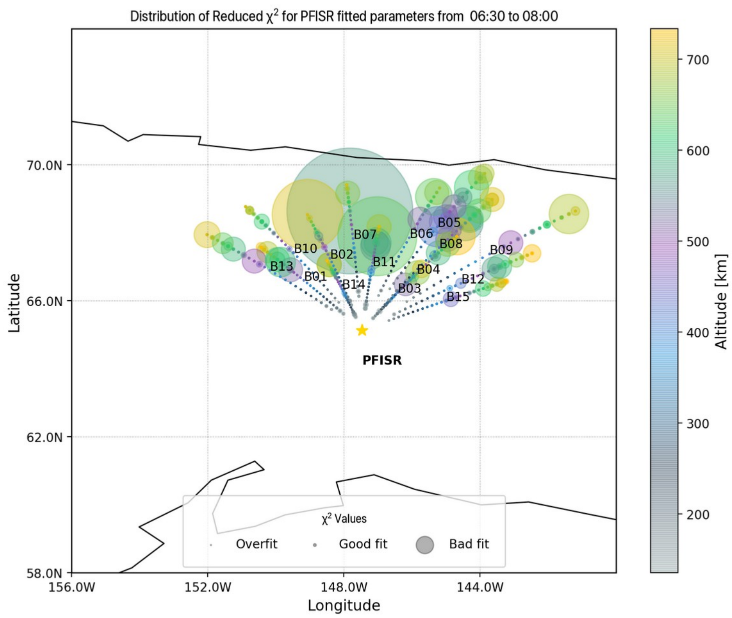

Figure 8. The distribution of the reduced χ^2 values along the PFISR beams between 0630-0800 UT are plotted. The colors denote the altitude where the χ^2 values are shown.

(0.1 − 10), and Bad fit (> 10). As can be seen from the distribution presented in Figure 8, there are certain Beams, i.e: 5, 8, 13, that are more prone to bad estimates, as well as certain altitudes, i.e: above 450 km.Therefore, beams with smaller reduced χ^2 distributions (Beam-04 for east, 14 for west and 11 for center) and the altitude profiles below 450 km are chosen for model validation throughout the paper.

3 Results

Below we discuss modeling results for several I-T parameters (electron density, electron temperature, and ion temperature) and compare them with PFISR measurements along the beams. Figure 9 illustrates the change in electron density between 0630 to 0800 UT along different beams. It is important to note that beams have different geometries, which leads to different sampling altitudes among different beams. In order to compare similar regions, the altitudes closest to 160 km (top), 250 km (middle) and 320 km (bottom) were picked. The gray dotted lines show the PFISR measurements, whereas the gray shaded regions show the range of errors associated with the measurements. The errors increase with the altitude. The simulated electron density profiles are mostly within the measured range showing a tendency for underestimation, especially at altitudes above 150 km. The measurements show rapid changes which are not well captured with the simulation results. Especially the 162 km profile along Beam 11 shows enhancements around 0640 to 0650 UT, 0705 to 0725 UT, and 0740 to 0750 UT with multiple minute-to-minute peaks. At 245 km along Beam 11, the modeled results perform well for capturing the overall trend of electron density, however failed to reproduce the peaks between 0639-0650, 0705-0720 and 0740-0755 UT. The difference between modeled responses are more obvious at 160 km profile. The GITM-HIME[V] and GITM-HIME[T] results showed a drop between 0700 to 0710 UT, followed by an enhancement around $0.5 \cdot 10^{11} m^{-3}$ around 0720 UT, whereas the GITM[W] and GITM-HIME[B] results didn't show the drop and the enhancement.

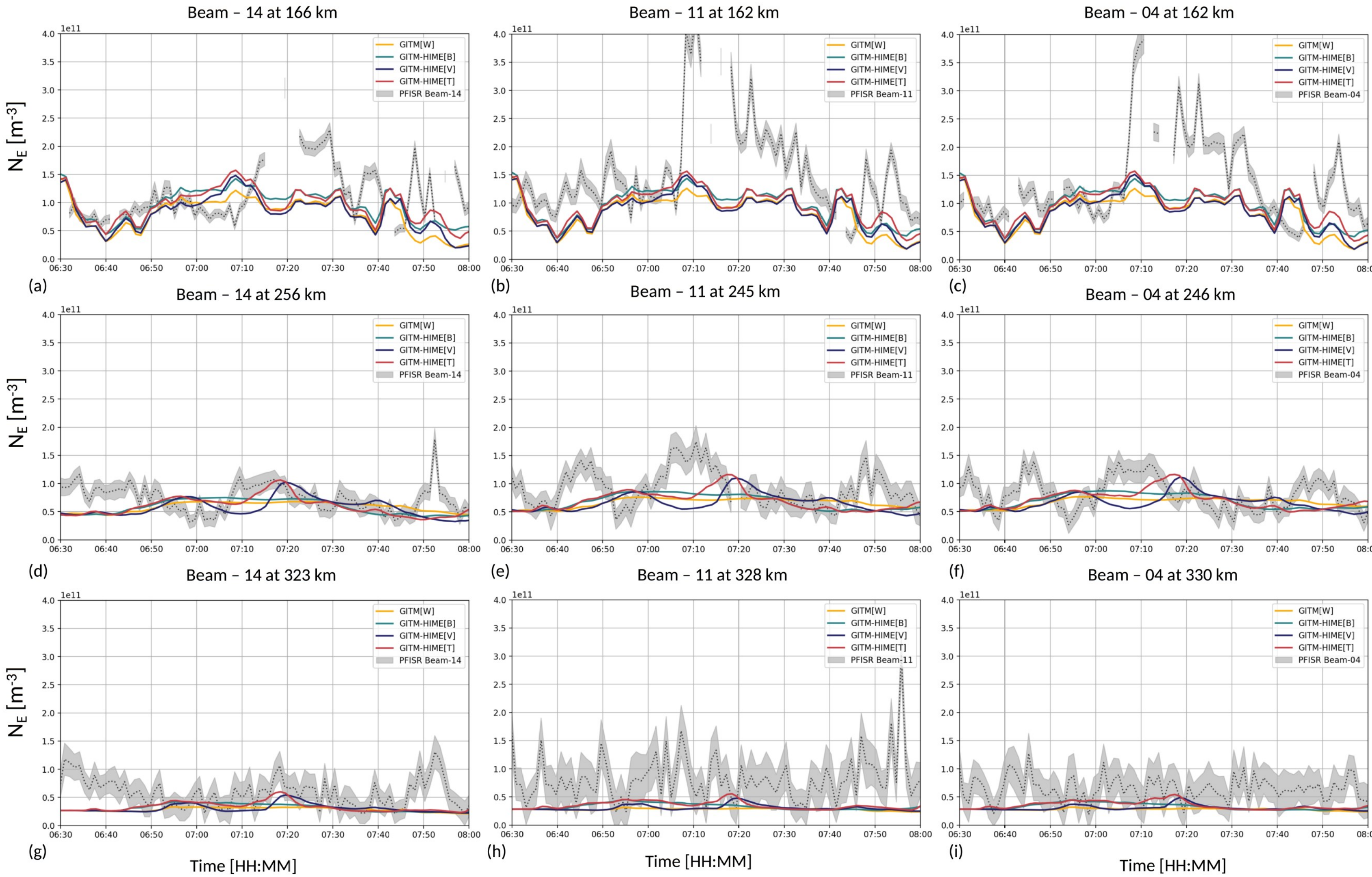

Figure 9. The temporal variation of the PFISR estimated and modeled electron densities are shown between 0630-0800 UT for Beam-14 (left column), Beam-11 (middle column) and Beam-04 (right columnt). The gray lines show PFISR measurements, the yellow (GITM[W]), green (GITM-HIME[B]), blue (GITM-HIME[V]), and red (GITM-HIME[T]) lines show simulated responses. The panels show responses extracted at ˜160 km (a,b,c), at ˜250 km (d,e,f) and ˜320 km (g,h,i).

Figure 10 shows the evolution of the electron temperature between 0630 to 0800 UT, along Beams 4, 11 and 14 at altitudes close to 160, 250, and 320 km.The electron temperature does not change significantly between different altitudes or beams. Especially along Beam 11, the simulated electron temperatures captures the overall trend of the measurements well, except for overestimating the values around 500 K between 0718-07226 UT at 160 km. The electron temperature preserves the same variability but increases in magnitude with altitude. The variability seen in electron temperature data is around 2 minutes, which is closer to the lower limit of the meso-scale interval. Overall, the meso-scale drivers do not alter the simulated electron temperatures considerably.

The change in ion temperature between 0630 to 0800 UT, is shown in Figure 11 in a similar manner to Figures 9 and 10. In general, ion temperature decreases with altitude. The profiles in Figure 11b demonstrates the key differences between drivers. The GITM-HIME[B] and GITM-HIME[T] captures the overall trend of the measurements, especially for the peaks at 0707 UT and 0743 UT, where GITM[W] and GITM-HIME[V] results don't compare well. All four simulation results fail to capture the peak at 0639 UT. It is important to note that ion temperature results with GITM-HIME[B] have a higher magnitude, whereas the GITM-HIME[V] results are more dynamic. Both behaviors, increased magnitude and variability, can be seen in GITM-HIME[T] ion temperature profiles.

Figure 12 illustrates the three components of ion convection velocities, East-West (top), North-South (middle), and Vertical (bottom), between 0630-0800 UT at three different latitudes, 66°, 68°, 70° along PFISR longitude. The gray lines show the PFISR 2D estimated velocities extracted at the same locations, and the same color codes are preserved for simulation results which are extracted at 250 km. Figure 12a shows both the GITM-HIME[V] and GITM-HIME[T] simulations capture the peaks and variability of the estimated velocity measurements very well, however there is no clear winner throughout the interval. Simulations driven with GITM[W] potentials do not show significant variations in time, remaining constant around -500 m/s. Figure 12d shows the North-South component of the velocity. Both GITM-HIME[V] and GITM-HIME[T] simulations capture the magnitude and variability of the estimated velocities very well, except for a brief interval between 0655-0710 UT. The North-South component of the velocity tended to be smaller than the East-West component, however it became larger after 0745 UT. The vertical component of the velocity shown in Figure 12g is the smallest component of the velocity. Similarly, the GITM-HIME[V] and GITM-HIME[T] simulations outperformed the GITM-HIME[B] and GITM[W] simulations. Likewise, the simulated East-West velocities compared at 68 ° demonstrated the GITM-HIME[V] and GITM-HIME[T] simulations captured the variability and enveloped the magnitude very well as shown in Figure 12b. Both the North-South and Vertical components shown in Figures 12e and h were underestimated around the peaks at 0635, 0655, 0715, and 0725 UT. The Figure 12c shows the East-West velocity extracted at 70, close to the upper boundary of the domain. The GITM-HIME[T] simulation results outperform the others in comparison to estimated velocity. Both the GITM-HIME[V] and GITM-HIME[T] simulations capture variability but miss the magnitude in North-South component shown in Figure 12f. As for the vertical velocity in Figure 12i, the GITM-HIME[V] simulation results had the best agreement with the estimated velocity.

To understand how the simulated neutral winds are affected by the meso-scale electric fields, the neutral wind velocities around 250 km altitude are compared with the measured neutral winds at the SDI sites, Eagle (left column), Poker Flat (middle column) and Toolik (right column) as shown in Figure 13. At the Eagle site, measured neutral wind velocities were around 50 m/s westward (Figure 13a) and around 25 m/s southward (Figure 13d). The simulated velocities were larger, around 100 m/s westward, but gradually decreased to 40 m/s towards the end of the interval. However, the simulation results showed initial northward velocities around 75 m/s dropping to 65 m/s around 0800 UT. At the Poker site, both the observed and the simulated velocities were westward ranging between 100 to 50 m/s (Figure 13b). Similar to the comparison with the Eagle site observations, the sim-

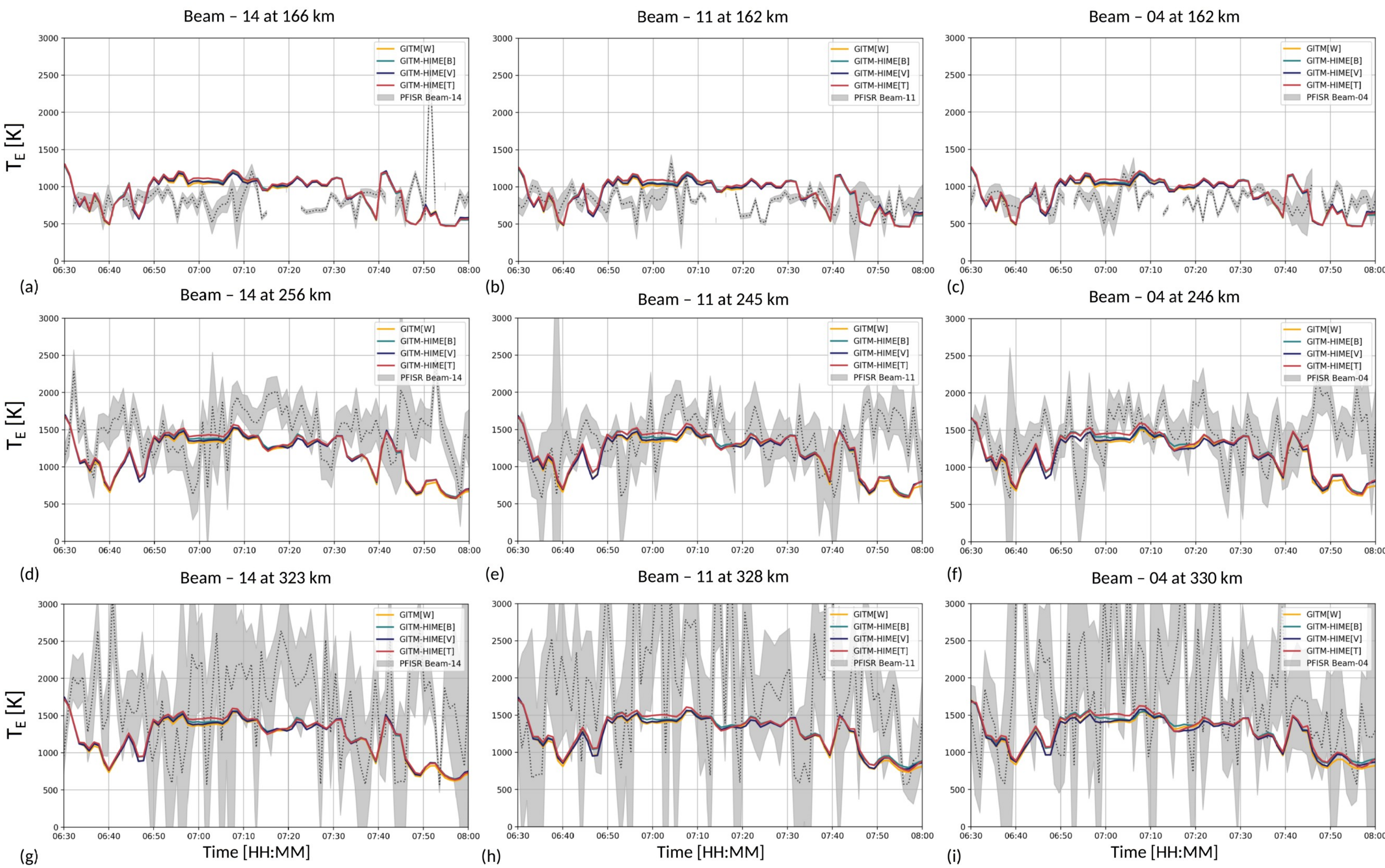

Figure 10. The temporal variation of the PFISR estimated and modeled electron temperatures are shown between 0630-0800 UT for Beam-14 (left column), Beam-11 (middle column) and Beam-04 (right column). The gray lines show PFISR measurements, the yellow (GITM[W]), green (GITM-HIME[B]), blue (GITM-HIME[V]), and red (GITM-HIME[T]) lines show simulated responses. The panels show responses extracted at ˜160 km (a,b,c), at ˜250 km (d,e,f) and ˜320 km (g,h,i).

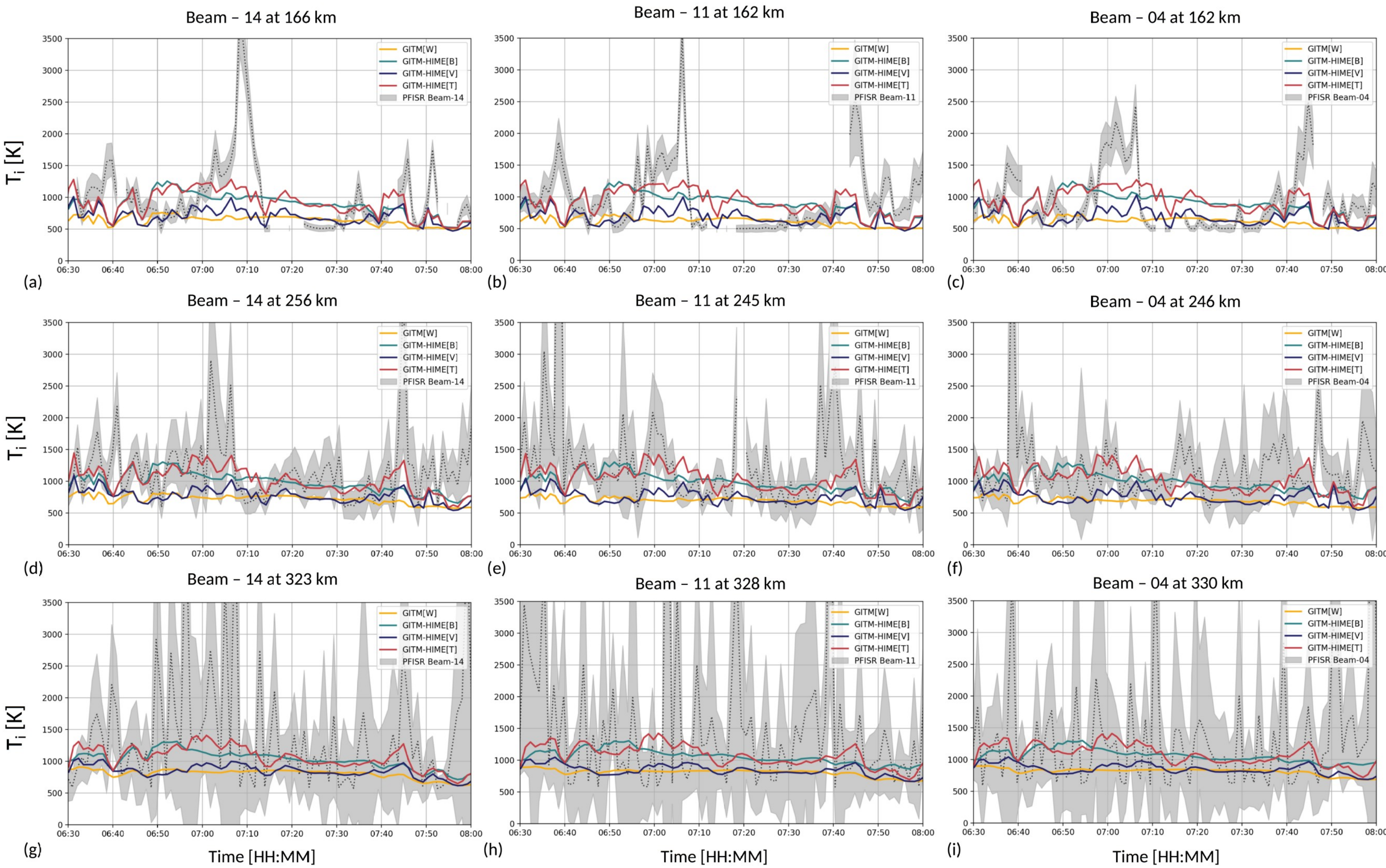

Figure 11. The temporal variation of the PFISR estimated and modeled ion temperatures are shown between 0630-0800 UT for Beam-14 (left column), Beam-11 (middle column) and Beam-04 (right column). The gray lines show PFISR measurements, the yellow (GITM[W]), green (GITM-HIME[B]), blue (GITM-HIME[V]), and red (GITM-HIME[T]) lines show simulated responses. The panels show responses extracted at ˜160 km (a,b,c), at ˜250 km (d,e,f) and ˜320 km (g,h,i).

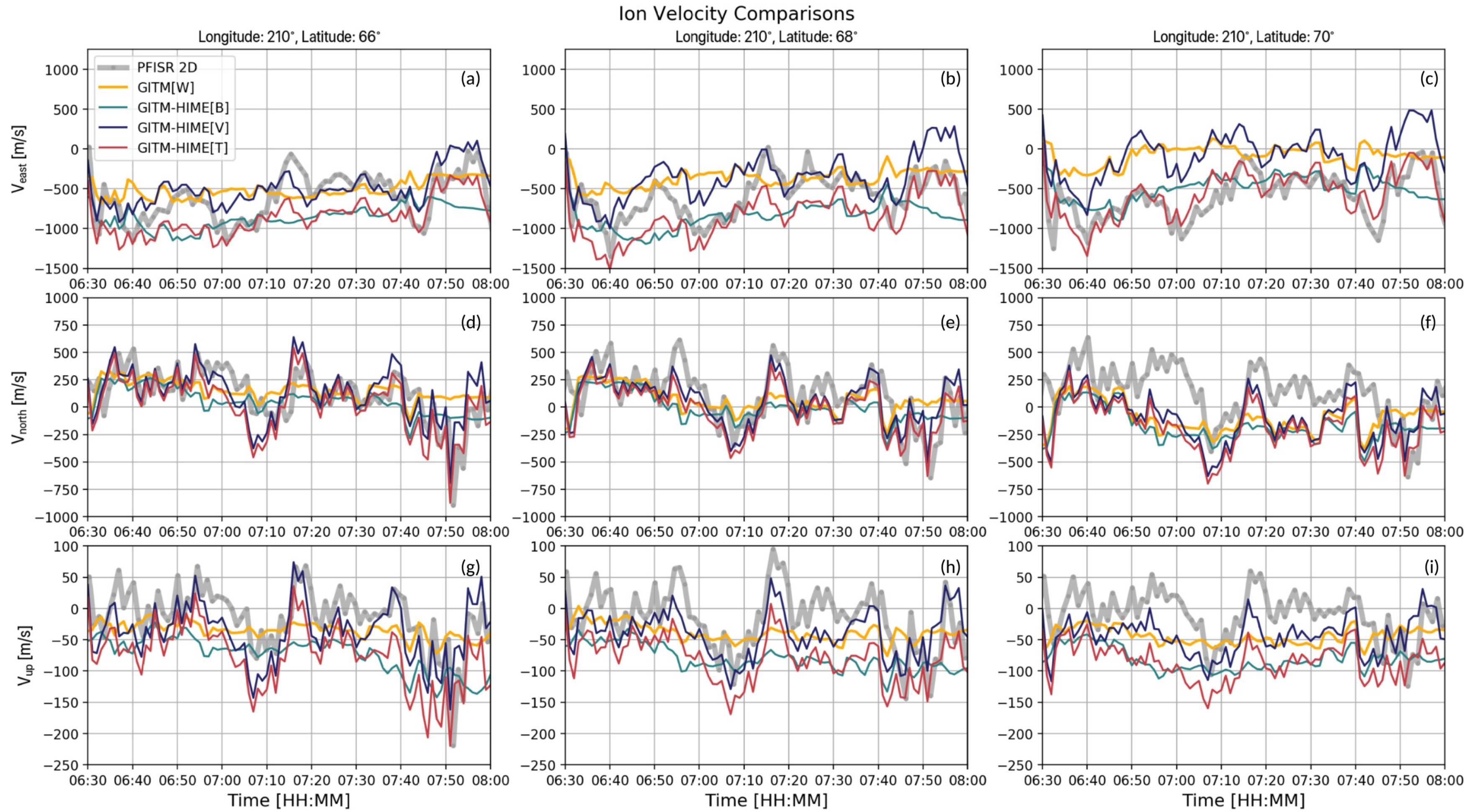

Figure 12. The temporal variation of the modeled and estimated ion velocity components are shown between 0630-0800 UT. The gray lines show PFISR 2D velocity estimates, tthe yellow (GITM[W]), green (GITM-HIME[B]), blue (GITM-HIME[V]), and red (GITM-HIME[T]) lines show simulated responses. The upper panels show east-west (a,b,c), middle panels (d,e,f) show north-south and bottom panels (g,h,i) show upward components of ion velocity. The left column (a,d,g) show velocities taken from 210° longitude, 66° latitude, middle column (b,e,h) values are taken from 210° longitude, 68° latitude, and the values on the right column (c,f,i) are taken from 210° longitude, 68° latitude.

ulations mischaracterized the neutral wind as northward whereas measurements indicated southward flows (Figure 13e). At the Toolik site, neutral wind measurements indicated mostly southward flows with speeds ranging from -20 to 60 m/s (Figures 13 c and f), however simulations indicated strong neutral wind in the northwest direction. The vertical component of the neutral wind was slow and mostly fluctuated around zero in all three sites (Figures 13g, h, and i). Although, the simulation responses didn't differ much throughout the period, GITM-HIME results for northward velocity started to diverge from GITM[W] results around 0639 UT, resulting in an average of 5 m/s difference in magnitude onwards. Similar behaviour was seen in Toolik and Eagle sites as well. [c1]For the studied interval the east-west components of the neutral winds are aligned with the ion convection profiles shown in Fig 12. However, the modeled neutral winds do not show the same variability displayed by ion convection profiles.

4 Discussion

4.1 Sources of Discrepancies

The ion convection comparisons of PFISR estimates with the GITM-HIME[V] and GITM-HIME[T] simulations demonstrated promising results for the presented meso-scale electric field variability modeling approach.The data-model comparisons of the electron density, electron and ion temperatures along the PFISR beams showed some disagreements. Among compared quantities, the simulated neutral wind profiles showed the most discrepancy compared to the observations, in addition to a very small response to the meso-scale drivers. A detailed study on thermospheric weather simulations was conducted Harding et al. (2019). Their results demonstrated that GITM simulations of neutral winds only showed limited spatial variability and had a low correlation factor compared with the observations. Therefore, we conclude that the poor agreement with the modeled and observed neutral winds, is not immediately related to the scale of the driving. [c1]However, recent results by Zou et al. (2018) showed that meso-scale F region winds respond to transient nightside plasma flows, and the responsiveness could be explained with strong ionization and enhanced electron density associated with auroras. The remainder of this subsection will focus on the electron density response.

To understand the reasons for the disagreement in simulated and observed electron densities, we will first look at the comparisons illustrated in Figure 9b and e, in which the time series of data from Beam 11 at 162 km and 245 km altitudes were displayed. The PFISR electron density measurements showed some minute-to-minute changes, however there were three intervals of enhancement that was consistent between these two altitudes. These intervals were between 0640 to 0650 UT, 0705 to 0725 UT, and 0745 to 0755 UT. One possible explanation for the underestimated electron density is the meso-scale electron precipitation that might have occurred during these intervals.

Figure 14 shows the Poker Flat DASC green (top row) and red (bottom row) line images between 0630-0650 UT. The green line images shows a significant enhancement in intensity, exceeding 1000 Rayleighs, between 65° to 70° latitudes and 210° to 220° longitudes at 0640 UT. At 0645 UT, the enhancement is confined in a narrow band located at the northeast corner and the intensity starts to diminish by 0650 UT. The red line profiles shown in bottom row does not demonstrate a significant variation. The intensity enhancements seen in red line images were around 300 Rayleigh. The second interval is displayed in Figure 15. The green line images showed multiple arc like formations between 0705 to 0720 UT. At 0705 UT, with the peak intensity centered around 66° latitude and 221° longitude. At 0710 UT, the peak intensity was located around 68° latitude and 210° longitude. At 0715 and 0720

[c1] *DSO*: *Text added.*
[c1] *DSO*: *Text added.*

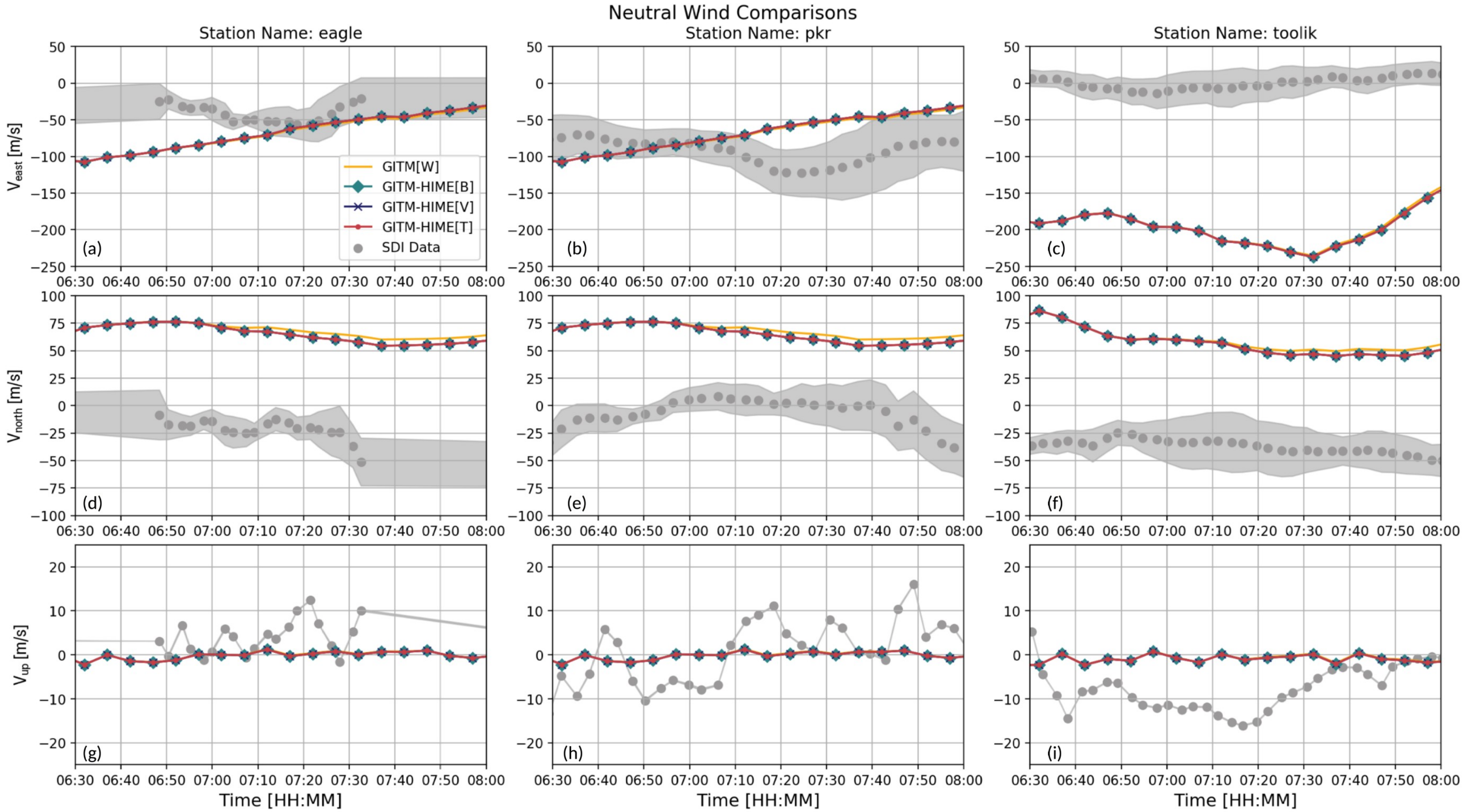

Figure 13. The temporal variation of the modeled and observed neutral velocity components are shown between 0630-0800 UT. The gray lines show SDI neutral velocity measurements, the yellow (GITM[W]), green (GITM-HIME[B]), blue (GITM-HIME[V]), and red (GITM-HIME[T]) lines show simulated responses at 250 km. The upper panels show east-west (a,b,c), middle panels (d,e,f) show north-south and bottom panels (g,h,i) show upward components of neutral velocity. The left column (a,d,g) show velocities taken from Eagle Site, middle column (b,e,h) values are taken from Poker Site, and the values on the right column (c,f,i) are taken from Toolik Site.

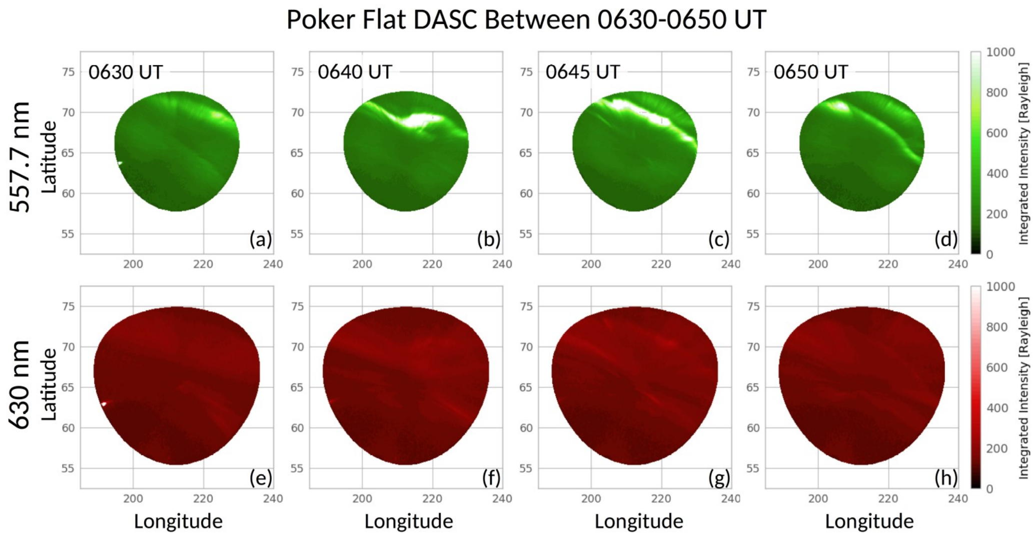

Figure 14. The Poker Flat DASC images corresponding to the first peak seen in PFISR Beam-11 data are shown. The images show green and red line emissions at 0630 (a and e), 0640 (b and f), 0645 (c and g), and 0650 UT (d and h).

UT, the main arc started to diminish. The red line images on the bottom row of Figure 15 showed a persistent, narrow arc with a lower intensity around 400 Rayleigh, spanning through 70° to 65° latitude of the DASC FOV. The third interval between 0740 to 0755 UT was very dynamic as displayed in Figure 16. The green line emissions were strong, exceeding 1000 Rayleigh, and peaked at 0745 and 0750 UT, spanning a wide range in latitude and longitude. These peaks were visible in the red line images, with intensity enhancements around 700 Rayleigh. Overall intensity of the auroral features seen in green line images were higher from the red line images. The green line images correspond to [c2]100-150 km altitude, whereas the red line images correspond to 250 km altitude. The PFISR electron density measurements for Beam-11 shown in Figure 9b and and e also showed differences based on altitude, where the enhancement in the 162 km profile was significantly larger than the enhancement in the 245 km profile. The video showing the temporal evolution of the visible aurora with Poker Flat DASC 427.8 nm is not discussed here, since this line corresponds to lower altitudes (100 km).

The dynamic features shown in Figures 14, 15, and 16 indicate significant electron precipitation at meso-scales (Syrjäsuo & Donovan, 2002; Nishimura et al., 2010), supported by the rapid changes in time. However, the Ovation model used to drive GITM and GITM-HIME, is a large-scale precipitation model and can not resolve these meso-scale precipitation features. The electric fields and auroral precipitation are known to have an inverse relationship at auroral region (Evans et al., 1977) and their self-consistent treatment is crucial to further understand the meso-scale variability in the I-T system.

Not accounting for the meso-scale precipitation of energetic particles may also result in mischaracterization of the electron temperature profiles shown in Figure 10. The enhanced electron temperature changes the electron density profile through production and transport. Since the electron production due to photoionization remains the same and the meso-scale precipitation is not accounted for in all four simulations, the electron temperature doesn't change between different runs, resulting in similar photoionization, radiative, and dissocia-

[c2] *DSO*: ~~100 km~~

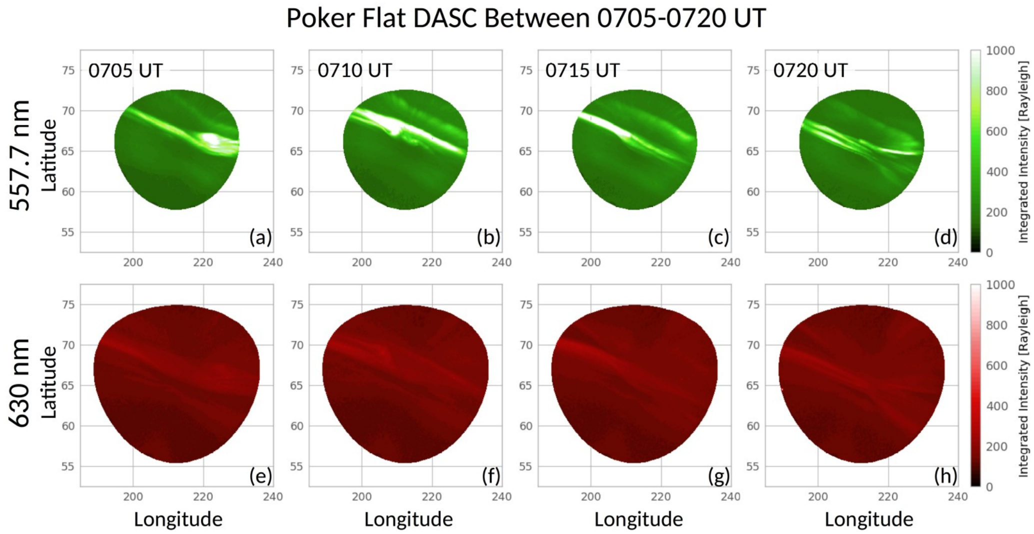

Figure 15. The Poker Flat DASC images corresponding to the second peak seen in PFISR Beam-11 data are shown. The images show green and red line emissions at 0705 (a and e), 0710 (b and f), 0715 (c and g), and 0720 UT (d and h).

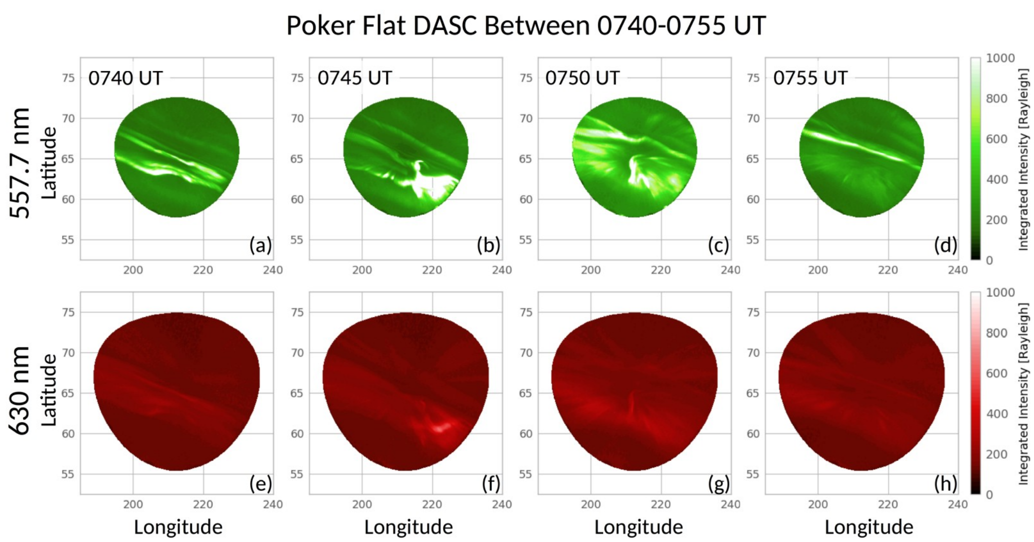

Figure 16. The Poker Flat DASC images corresponding to the third peak seen in PFISR Beam-11 data are shown. The images show green and red line emissions at 0740 (a and e), 0745 (b and f), 0750 (c and g), and 0755 UT (d and h).

tive recombination rates for electrons. Although the change in simulated electron density can not be attributed solely to chemical production, transport can explain the differences among HIME-driven responses between 0700-0730 UT shown in Figure 9e. We calculate the electron density change rate at 250 km due to transport in east-west and north-south directions as discussed in Meng et al. (2016). To account for the east-west transport the change in electron momentum flux is calculated between the east-west boundaries of the PFISR domain where the drivers were altered. Similarly, to calculate the north-south transport rates the electron momentum flux change between the north-south boundaries of the PFISR domain were used. The expressions used in calculating the rate of change in electron density due to transport terms are shown in Equations 8 and 9.

$$\left(\frac{dn_e}{dt}\right)_{ew} = \frac{< nV >_{east} - < nV >_{west}}{\Delta x} \tag{8}$$

$$\left(\frac{dn_e}{dt}\right)_{ns} = \frac{< nV >_{north} - < nV >_{south}}{\Delta y} \tag{9}$$

Here n_e shows the electron density, V was taken as the ion velocity, and <> denote averages along the boundaries. Δx and Δy correspond to the height (maximum latitude-minimum latitude) and width (maximum longitude-minimum longitude) of the PFISR domain.

Figure 17 shows the temporal evolution of the east-west (a) and north-south (b) transport rates inside the PFISR domain. The east-west transport rates are an order of magnitude higher than the north-south transport rates, owing to the strong northward electric fields, and westward ion convection. Around 0656 UT, the GITM-HIME[V] transport rates start to increase in the westward direction, followed by a decrease at 0701 UT. This decrease was also seen in GITM-HIME[T] transport rates until 0716 UT. The increase and decrease in GITM-HIME[V] westward transport explains the decrease and increase seen in the GITM-HIME[V] electron density (Figure 9e) profile. Similarly the decrease in GITM-HIME[T] transport coincides with the increase seen in the corresponding electron density (Figure 9e) profile.

4.2 Evaluation of Ion to Neutral Energy Transport Terms

The ion temperature peaks didn't compare well with the observed peaks. Investigating Figure 11e in detail shows that the addition of variability improves the estimates of ion temperature peaks, whereas including the background potentials corrects the trend and magnitude of simulation results. In order to understand the ion temperature behaviour, the factors contributing to the temporal variation of the ion temperature in GITM should be considered. The contributions from the collision and frictional terms in the energy transfer equation are shown in Equation 10.

$$\frac{dT_i}{dt} = \sum_i \frac{1}{\rho C_p} \frac{n_i m_i \nu_{in}}{m_n + m_i} \, 3k_B (T_n - T_i) + m_n (u_n - v_i)^2 \tag{10}$$

Here ρ denotes mass density, C_p is the heat capacity, n is the number density, m is the mass, ν_{in} is the ion-collision frequency, k_B is the Boltzmann coefficient, T is the temperature, while u_n and v_i denote the neutral and ion velocities. The i and n subscripts refer to ions and neutrals. In the results section, we have discusses that the missing electron precipitation may be responsible for the disagreement between the observed and simulated electron density responses. Neutral wind observations and simulations also showed disparities, further playing into the mischaracterization of ion temperature.

Despite the underestimated ion temperatures the model results are still useful in understanding the coupling between I-T systems. For large-scale and quasi-static structures at

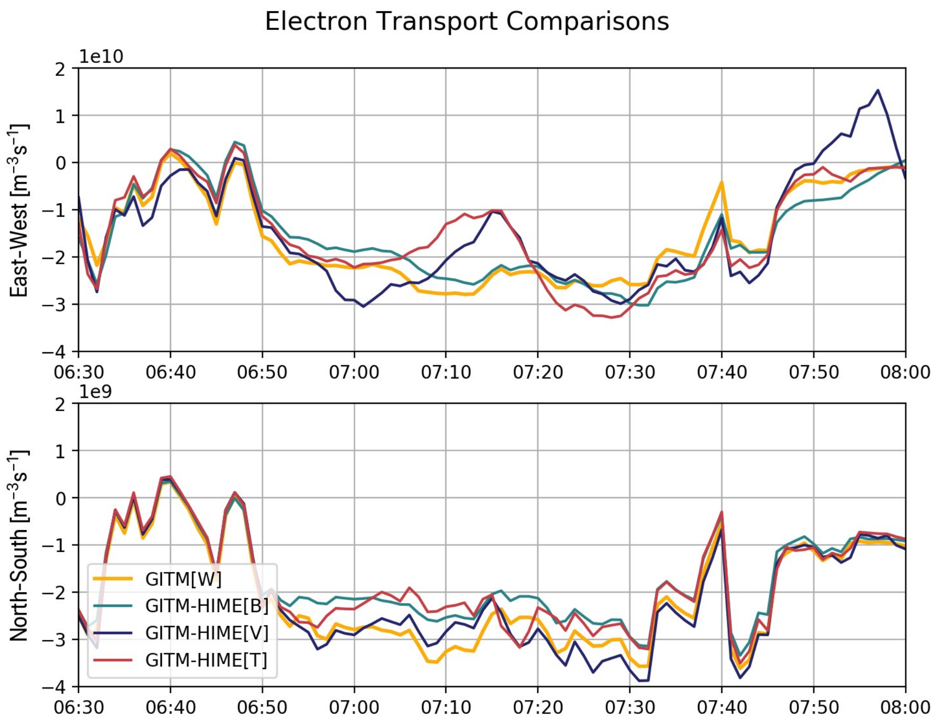

Figure 17. The east-west (a) and north-south (b) components of the electron transport are plotted in between 0630-0800 UT. The the yellow (GITM[W]), green (GITM-HIME[B]), blue (GITM-HIME[V]), and red (GITM-HIME[T]) lines show simulated responses.

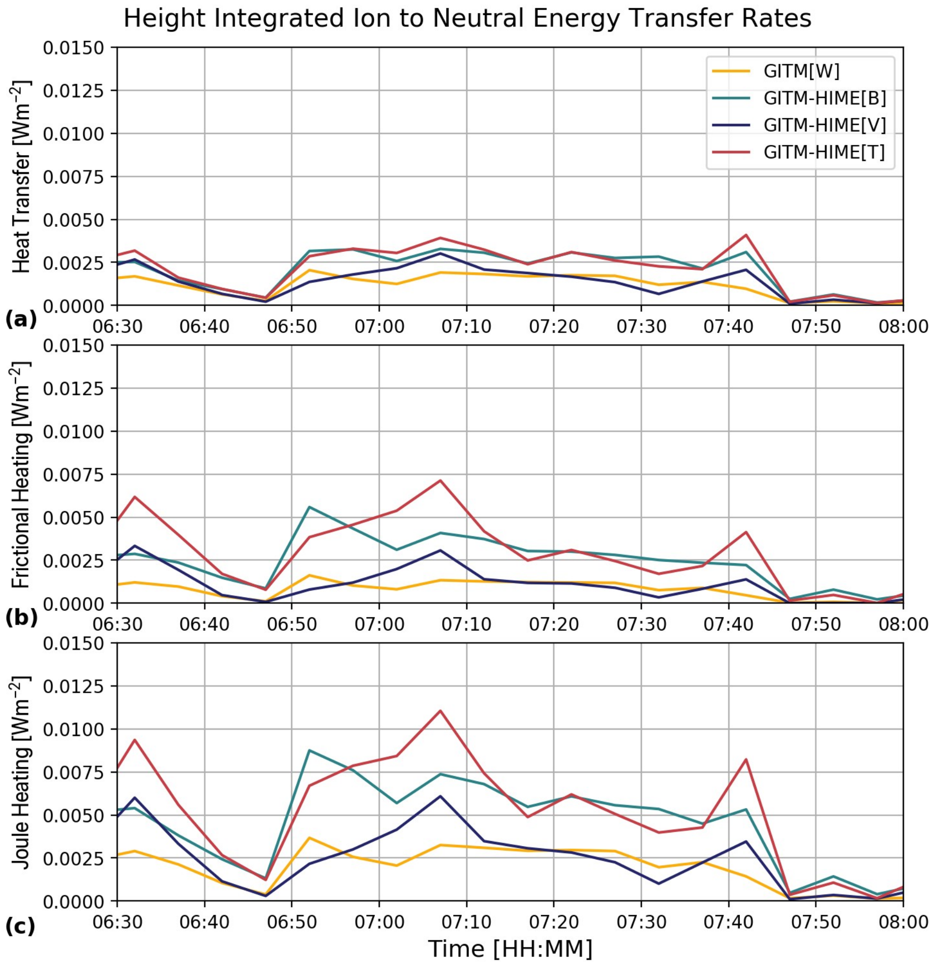

Figure 18. The ion to neutral heat transfer (a), frictional heating (b), and Joule heating (c) rates are plotted in between 0630-0800 UT. The yellow (GITM[W]), green (GITM-HIME[B]), blue (GITM-HIME[V]), and red (GITM-HIME[T]) lines show simulated responses.

high-latitudes, the ion-to-neutral heat transfer rate ($3k_B(T_n - T_i)$ term) and the ion-neutral frictional heating rate ($m_n(u_n - v_i)^2$) can be assumed equal ((Thayer & Semeter, 2004), (Schunk & Nagy, 2009), (J. Zhu et al., 2016)). Following the definition of J. Zhu et al. (2016), the Joule heating rate is treated as the complete neutral to ion collisional energy transfer rate as shown in Equation 11.

$$\frac{dE_i}{dt} = \sum_i \frac{n_i m_i \nu_{in}}{m_n + m_i} \; 3k_B(T_n - T_i) + m_n(u_n - v_i)^2 \tag{11}$$

Figure 18 shows height-integrated ion to neutral heat transfer, frictional heating and Joule heating transfer rates calculated at every 5 minutes for four simulations. The heat transfer profile displays a peak around 0632 UT, followed by a drop. The transfer rate increases again around 0647 UT and stays around 0.003 W/m^2 until 0747 UT. The GITM-HIME[B] and GITM-HIME[T] simulations produce heat transfer rates that are around 0.002 W/m^2 higher than GITM[W] simulations between 0647 UT to 0737 UT, followed by a peak of 0.004 W/m^2 that GITM[W] missed. The frictional heating rate (Figure 18b) for

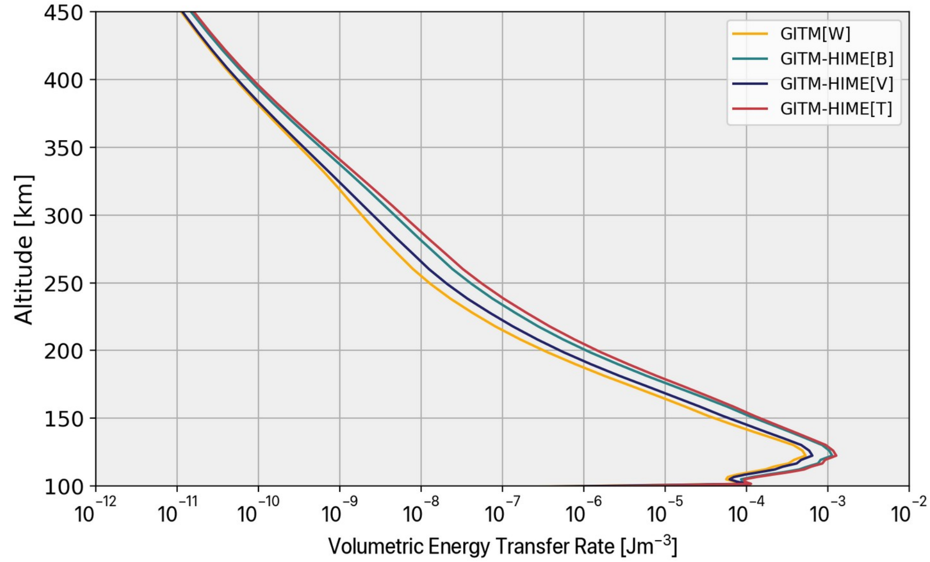

Figure 19. The vertical profile of ion to neutral volumetric energy transfer rates integrated between 0630-0800 UT are demonstrated. The yellow (GITM[W]), green (GITM-HIME[B]), blue (GITM-HIME[V]), and red (GITM-HIME[T]) lines show simulated responses.

GITM[W] does not vary significantly compared to the heat transfer rate. On the other hand, the GITM-HIME[B], GITM-HIME[V] and GITM-HIME[T] simulations all produce higher frictional heating rates. The Joule heating rate, which is treated as the sum of ion to neutral heat transfer and frictional heating rates, is shown in Figure 18c.It follows a similar trend to the frictional heating rate profile. Overall, the GITM-HIME[V] and GITM-HIME[T] rates produce three peaks at 0632 UT, 0707 UT, and 0742 UT. These enhancements all coincide with the increased ion temperature shown in Figure 11e.Altogether, both height-integrated heat transfer, frictional and Joule heating rates significantly differ from the GITM[W] results when more realistic drivers are employed. It is also important to note that the highest contribution to the height-integrated energy transfer rates comes from altitudes below 150 km during the entire period.

Figure 19 illustrates the altitude profile of the total ion to neutral volumetric energy transfer (Joule heating) rates obtained from the simulations. It can be seen that the GITM-HIME[T] and GITM-HIME[B] simulations resulted in higher energy transfer rates starting from 110 km compared to GITM[W] simulations. This difference became especially more pronounced between 180-300 km, where the GITM-HIME[V] energy transfer rates were twice the magnitude of GITM[W] transfer rates. These results yield an average enhancement of 30 nW/m^{-3} in GITM-HIME[V], 110 nW/m^{-3} in GITM-HIME[B], and 140 nnW/m^{-3} in GITM-HIME[T] simulations compared with the GITM[W] results at 120 km. Likewise the Alfv´enic heating study conducted by Lotko and Zhang (2018), found the heating due to variability (66 mV/m) around 10 nW/m^{-3}, and due to a quasi-static field (similar to our GITM-HIME[B] approach) around 38 nW/m^{-3} higher than the simulated response with a Weimer type electric field at the same altitude. The simulated values at F region altitudes follow a similar trend, however the magnitudes are very low due to nighttime electron densities to be compared directly. Verkhoglyadova et al. (2018) estimated the energy deposition to reach about 10% of the overall energy budget calculated with a static field around 250 km at high-latitudes. In this study we have shown the energy deposited from ions to neutrals increased by 1.7 times for the GITM-HIME[V], 3.1 for the GITM-

HIME[B] and 4.5 for the GITM-HIME[T] simulations compared to GITM[W] at the same altitude. Ultimately, the meso-scale electric fields deposit more energy locally than the large-scale electric fields. The overall energy deposited can depend on magnetic local time, latitude, and magnitude of the fluctuations.

4.3 Future work

This study makes use of various empirical and physical relations, assumptions, approximations, numerical methods, observations and fitted data. As detailed in this paper, there are certain discrepancies that arise between the modeled behaviour and the observations. We can understand some of these discrepancies better by categorizing them according to their reducibility as epistemic and aleatory (Choi et al., 2006). Epistemic uncertainties arise from the lack of or incomplete understanding of the underlying physical processes. The missing meso-scale particle precipitation in the model is a good example of the epistemic uncertainty. The Poker Flat DASC images (Figures 14, 15, and 16) have shown a significantly different auroral structure compared to what the OVATION model can produce. [c1] Previous studies on the auroral zone by Brekke et al. (1974) and Brekke and Hall (1988), demonstrated that Hall and Pedersen conductivities are significantly altered due to particle precipitation. Therefore, not accounting for meso-scale particle precipitation can result in significant mischaracterization of the conductance profiles. As suggested by Cosgrove et al. (2009), the independent treatment of conductance and electric fields can lead to indefinite conclusions on whether Joule heating is over or underestimated by numerical models. Future work to merge the empirical large-scale precipitation model with the meso-scale particle precipitation, will significantly elevate the modeling effort presented.

Another source of epistemic uncertainty comes from the numerical method used to calculate and merge new potentials with the Weimer potentials as discussed in Section 2.2. We provided an error analysis in Figure 5 before the potentials were merged and showed that the errors we introduce with this method were on the order of 10^{-1} mV/m in x, and 10^{-2} mV/m in y components of the electric field. Even though the Weimer potentials do not show significant change over the PFISR area that we modified, we still expect the errors to increase after the two potentials are added as shown in Figure 7. Finally, the Gaussian filter applied at the boundary of the PFISR domain for a smooth blending alters the potentials and adds to the electric field errors.

In addition to the epistemic uncertainties in the model, there are aleatory uncertainties that can not be immediately remedied. The aleatory uncertainties emerge from the measurement discrepancies, computation errors, lack of data and coverage. We identified the sources of these uncertainties as PFISR observations, fitted data, and other numerical assumptions in GITM. Among these, the PFISR observations and fitted data are the most prominent sources of uncertainty. Cosgrove and Codrescu (2009) suggested that there were two kinds of model error with different characteristics, namely the resolved-scale model uncertainty and the small-scale electric field variability. While the errors introduced by grid resolution constitute the resolved-scale model uncertainty, the PFISR estimates introduce further small-scale electric field uncertainties to the study. These measurements were obtained during nighttime at F region altitudes during low electron densities, resulting in low signal to noise ratios. These measurements were then fitted to a 2D grid (Nicolls et al., 2014), where the aleatory uncertainties further propagated to the final electric field product. The goodness of the fit parameter, which assesses whether or not the fitting model was appropriate (Press et al., 2007) was shown in Figure 8. These values deviate from the optimum value of 1 around the top, left and right boundaries, above 450 km altitude, introducing uncertainties to the upper boundary driver of GITM. A recent study by Chen et al. (2018) on investigating the role of uncertainties in electric field boundary conditions to

[c1] *DSO: Text added.*

determine cross polar cap potential values revealed that epistemic uncertainties play a bigger role in the performance of their physical model. Morley et al. (2018) examined how the uncertainties in the solar wind input affect the ground magnetic perturbations and found various intervals that can be explained by the propagation of driver uncertainty. As the uncertainty quantification is becoming an integral part of space weather studies (Knipp et al., 2018), we plan to further evaluate the model performance with ensemble simulations accounting for the electric field errors. A future work will be conducted with a set of electric fields populated through a probability density function within the bounds of measurement errors using the same covariance matrix used for the fitting to run GITM.

The incorporation of the meso-scale electric fields in a global model was the first step of the HIME framework. As shown by this study, the crucial next development step for HIME is including the meso-scale particle precipitation information. The isinglassv3 experiment used in this study was designed to sample F region electric fields, however there are various PFISR modes, such as Themis36 and WorldDay40, which enable sampling E and F layers simultaneously using alternating codes and long pulses. With such experiments it is possible to obtain meso-scale electric field estimates as well as particle precipitation information. J. L. Semeter and Kamalabadi (2005) has demonstrated a technique for inverting ISR measurements to determine the electron energy spectrum, and later studies successfully applied the same inversion technique (Sivadas et al., 2017).Further case studies will be conducted to thoroughly validate the HIME framework using both meso-scale electric field and particle precipitation information.

5 Conclusions

We have developed and successfully implement a new framework that can convey local 2D measurements of high-latitude meso-scale electric fields as drivers in a global ionosphere thermosphere model. In the case study reported in the paper, HIME is constructed by combining the Weimer empirical model with regional estimates of dynamic electric field potential inferred from PFISR measurements. This approach was applied to modeling high-latitude nighttime I-T dynamics during 2 March 2017 with GITM. The choice of event was motivated by availability of a special multi-beam observational mode of PFISR. We designed four numerical experiments to understand the effects of multi-scale driving on the I-T system. The GITM simulations were driven with Weimer, Weimer merged with background, Weimer merged with variable, and Weimer merged with total electric field potentials. To validate our modeling effort, we conducted data-model comparisons with PFISR estimated ion velocity, as well as electron density, electron and ion temperatures along PFISR beams, and neutral wind data from SDIs. We inter-compared effects of large-scale and meso-scale driving on the I-T system.The modeling results agree reasonably well with observations given high levels of noise for several of the observed time series. There are also several notable discrepancies.We investigated the sources for temporal changes in plasma properties and quantified the amount of energy transferred from ions to neutrals by calculating the heat transfer rates. We concluded with a discussion on the limitations of the new framework and future directions of its development. The key findings of the paper are summarized below.

1. With the proposed framework, HIME, local electric field variability can be successfully conveyed to GITM.
2. Ion velocity variations are better captured by HIME-driven simulations.
3. Changes in simulated electron density for the modeled event are likely due to the horizontal transport mechanism, and the models do not reproduce the variability observed in the PFISR data.
4. We suggest the missing meso-scale particle precipitation is likely responsible for the underestimated electron density variations in the night-time high-latitude ionosphere.

5. Electron temperature measurements show rapid changes within 2 minutes. The simulated responses are somewhat underestimated and are not sensitive to the scale of [c1]electric field driving.
6. With meso-scale electric field driving, simulated ion temperature increases and becomes more dynamic.
7. The neutral wind velocities were not altered significantly through [c1]regional meso-scale driving.
8. The frictional heating rate is larger than the ion to neutral heat transfer rates when meso-scale drivers are used.
9. The deposited energy increases locally in HIME-driven simulations compared to Weimer-driven simulations above 110 km.
10. [c2]The meso-scale particle precipitation variations needs to be included to understand the effects of meso-scale variability on the I-T system.

Acknowledgments

This work was performed at the Jet Propulsion Laboratory, California Institute of Technology, under a contract with NASA. Sponsorship of the Heliophysics Division of the NASA Science Mission Directorate is gratefully acknowledged. J. L. Semeter was supported by NSF grant AGS-1821135. This material is based upon work supported by the Poker Flat Incoherent Scatter Radar which is a major facility funded by the National Science Foundation through cooperative agreement AGS-1840962 to SRI International. The authors gratefully acknowledge Aaron J. Ridley (University of Michigan) for providing the source code of GITM. The authors appreciate discussions with Michael D. Hartinger (Space Science Institute), Stephen R. Kaeppler (Clemson University), and Kristina A. Lynch (Dartmouth College, NH) for helpful references on rocket observations.The resources supporting this work were provided by the NASA High-End Computing (HEC) Program through the NASA Advanced Supercomputing (NAS) Division at Ames Research Center. The solar wind parameters and activity indices were taken from the OMNI database. The authors gratefully acknowledge Mark Conde for maintaining the SDI data at http://sdi_server.gi.alaska.edu/sdiweb/index.asp and ASI data at http://optics.gi.alaska.edu/optics/. We thank the developers of Spacepy (https://github.com/spacepy/spacepy.git), AACGMV2 (https://github.com/aburrell/aacgmv2.git), and Dascutils (https://github.com/space-physics/dascutils) libraries, which were used in this study. The dataset for this study consisting of the PFISR estimates and prepared simulation inputs can be accessed at NASA Open Data, https://open.nasa.gov/open-data/. The dataset has been cleared for Unlimited Release and we are currently in the process of archiving the data, which can be found at doi: To Be Assigned.

References

Ahn, B.-J., Robinson, R. M., Kamide, Y., & Akasofu, S.-I. (1983). Electric conductivities, electric fields and auroral particle energy injection rate in the auroral ionosphere and their empirical relations to the horizontal magnetic disturbances. *Planetary and Space Science*, *31* (6), 641-653. doi: 10.1016/0032-0633(83)90005-3

Balthazor, R. L., Moffett, R. J., & Millward, G. H. (1997). A study of the joule and lorentz inputs in the production of atmospheric gravity waves in the upper thermosphere. *Annales Geophysicae*, *15* (6), 779-785.

Birn, J., Drake, J. F., Shay, M. A., Rogers, B. N., Denton, R. E., Hesse, M., ... Prichett, P. L. (2001). Geospace environmental modeling (gem) magnetic re-

[c1] *DSO: Text added.*
[c1] *DSO: Text added.*
[c2] *DSO: Text added.*

connection challenge. *Journal of Geophysical Research*, *106* (A3), 3715-3719. doi: 10.1029/1999JA900449

Brekke, A., Doupnik, J. R., & Banks, P. M. (1974). Incoherent scatter measurements of e region conductivities and currents in the auroral zone. *Journal of Geophysical Research*, *79* (25), 3773-3790. doi: doi:10.1029/JA079i025p03773

Brekke, A., & Hall, C. (1988). Auroral ionospheric quiet summer time conductances auroral ionospheric quiet summer time conductances. *Annales Geophysicae*. doi: doi:1988AnGeo...6..361B

Brekke, A., & Kamide, Y. (1996). On the relationship between joule and frictional heating in the polar ionosphere. *Journal of Atmospheric and Terrestrial Physics*, *58*, 139-143. doi: 10.1016/0021-9169(95)00025-9

Chen, M. W., O'Brien, T. P., Lemon, C. L., & Guild, T. B. (2018). Effects of uncertainties in electric field boundary conditions for ring current simulations. *Journal of Geophysical Research: Space Physics*, *123*, 638-652. doi: 10.1002/2017JA024496

Choi, S.-K., Grandhi, R. V., & Cranfield, R. A. (2006). *Reliability-based structural design*. Springer.

Clayton, R., Lynch, K., Zettergren, M., Burleigh, M., Conde, M., Grubbs, G., . . . Varney, R. (2019). Two-dimensional maps of in situ ionospheric plasma flow data near auroral arcs using auroral imagery. *Journal of Geophysical Research: Space Physics*, *124*, 3036-3056. doi: 10.1029/2018JA026440

Codrescu, M. V., Fuller-Rowell, T. J., & Foster, J. C. (1995). On the importance of e-field variability for joule heating in the high-latitude thermosphere. *Geophysical Research Letters*, *22* (17), 2393-2396. doi: 10.1029/95GL01909

Conde, M., Craven, J. D., Immel, T., Hoch, E., Stenbaek-Nielsen, H., Hallinan, T., . . . Sigwarth, J. (2001). Assimilated observations of thermospheric winds, the aurora, and ionospheric currents over alaska. *Journal of Geophysical Research*, *106* (A6), 10493-10508. doi: 10.1029/2000JA000135

Conde, M., & Smith, R. W. (1995). Mapping thermospheric winds in the auroral zone. *Geophysical Research Letters*. doi: 10.1029/95GL02437

Connor, H. K., Zesta, E., Fedrizzi, M., Shi, Y., Raeder, J., Codrescu, M. V., & Fuller-Rowell, T. J. (2016). Modeling the ionosphere-thermosphere response to a geomagnetic storm using physics-based magnetospheric energy input: Openggcm-ctim results. *Journal of Space Weather and Space Climate*, *6* (A25). doi: 10.1051/swsc/2016019

Cosgrove, R. B., & Codrescu, M. (2009). Electric field variability and model uncertainty: A classification of source terms in estimating the squared electric field from an electric field model. *Journal of Geophysical Research*, *114* (A06301). doi: 10.1029/2008JA013929

Cosgrove, R. B., Lu, G., Bahcivan, H., Matsuo, T., Heinselman, C. J., & McCready, M. A. (2009). Comparison of amie-modeled and sondrestrom-measured joule heating: A study in model resolution and electric field–conductivity correlation. *Journal of Geophysical Research*, *114* (A04316). doi: 10.1029/2008JA013508

Cousins, E. D. P., & Shepherd, S. G. (2012). Statistical characteristics of small-scale spatial and temporal electric field variability in the high-latitude ionosphere. *Journal of Geophysical Research*, *117* (A03317). doi: 10.1029/2011JA017383

Crowley, G., & Hackert, C. L. (2001). Quantification of high latitude electric field variability. *Geophysical Research Letters*. doi: 10.1029/2000GL012624

Crowley, G., Hackert, C. L., Meier, R. R., Strickland, D. J., Paxton, L. J., Pi, X., . . . Wene, G. (2006). Global thermosphere-ionosphere response to onset of 20 november 2003 magnetic storm. *Journal of Geophysical Research*, *111* (A10S18). doi: 10.1029/2005JA011518

Deng, Y., Maute, A., Richmond, A. D., & Roble, R. G. (2009). Impact of electric field variability on joule heating and thermospheric temperature and density. *Geophysical Research Letters*, *36* (L08105). doi: 10.1029/2008GL036916

Deng, Y., & Ridley, A. J. (2006). Dependence of neutral winds on convection e-field, solar euv, and auroral particle precipitation at high latitudes. *Journal of Geophysical*

Research, *111* (A09306). doi: 10.1029/2005JA011368
Deng, Y., & Ridley, A. J. (2007). Possible reasons for underestimating joule heating in global models: E field variability, spatial resolution, and vertical velocity. *Journal of Geophysical Research*, *112*. doi: 10.1029/2006JA012006
Deng, Y., Zhu, Q., Lin, C. Y., Sheng, C., Zhao, Y., & Tsyka, J. (2019). Influence of meso-scale forcing on the ionosphere-thermosphere system: Gitm simulations. In *Sa51a - multiscale coupling and energy transfer in the magnetosphere-ionosphere-thermosphere-mesosphere system i.* https://agu.confex.com/agu/fm19/meetingapp.cgi/Paper/487717.
Dhadly, M. S., Meriwether, J., Conde, M., & Hampton, D. (2015). First ever cross comparison of thermospheric wind measured by narrow- and wide-field optical doppler spectroscopy. *Journal of Geophysical Research: Space Physics*, *120*, 9683-9705. doi: 10.1002/2015JA021316
Emery, B. A., Lathuillere, C., Richards, P. G., Roble, R. G., Buonsanto, M. J., Knipp, D. J., . . . Niciejewski, R. (1999). Time dependent thermospheric neutral response to the 2-11 november 1993 storm period. *Journal of Atmospheric and Solar-Terrestrial Physics*, *61*, 329-350. doi: 10.1016/S1364-6826(98)00137-0
Evans, D. S., Maynard, N. C., Trøim, J., Jacobsen, T., & Egeland, A. (1977). Auroral vector electric field and particle comparisons, 2 electrodynamics of an arc. *Journal of Geophysical Research*, *82* (16), 2235-2249. doi: 10.1029/JA082i016p02235
Fernandes, P. A., Lynch, K. A., Zettergren, M., Hampton, D. L., Bekkeng, T. A., Cohen, I. J., . . . Powell, S. P. (2016). Measuring the seeds of ion outflow: Auroral sounding rocket observations of low-altitude ion heating and circulation. *Journal of Geophysical Research: Space Physics*, *121*, 1587-1607. doi: 10.1002/2015JA021536
Forsyth, C., Rae, I. J., Mann, I. R., & Pakhotin, I. P. (2017). Identifying intervals of temporally invariant field-aligned currents from swarm: Assessing the validity of single-spacecraft methods. *Journal of Geophysical Research: Space Physics*, *122*, 3411-3419. doi: 10.1002/2016JA023708
Fujita, S., Tanaka, T., Kikuchi, T., Fujimoto, K., Hosokawa, K., & Itonaga, M. (2003a). A numerical simulation of the geomagnetic sudden commencement: 1. generation of the field-aligned current associated with the preliminary impulse. *Journal of Geophysical Research*. doi: 10.1029/2002JA009407
Fuller-Rowell, T. J., & Evans, D. S. (92). Height-integrated pedersen and hall conductivity patterns inferred from the tiros-noaa satellite data. *Journal of Geophysical Research*, *A7* (7606-7618). doi: 10.1029/JA092iA07p07606
Gjerloev, J. W., Ohtani, S., Iijima, T., Anderson, B., Slavin, J. A., & Le, G. (2011). Characteristics of the terrestrial field-aligned current system. *Annales Geophysicae*, *29*, 1713-1729. doi: 10.5194/angeo-29-1713-2011
Goodman, M. L. (1995). A three-dimensional, iterative mapping procedure for the implementation of an ionosphere-magnetosphere anisotropic ohm's law boundary condition in global magnetohydrodynamic simulations. *Annales Geophysicae*, *13* (8), 843-853. doi: 10.1007/s00585-995-0843-z
Grubbs, G. A., Zettergren, M. D., Samara, M., Michell, R., Hampton, D. L., Lynch, K. A., . . . Burleigh, M. (2017). Data-driven local-scale modeling of ionospheric responses to auroral forcing using incoherent scatter radar and ground-based imaging measurements. In *American geophysical union, fall meeting.*
Harding, B. J., Ridley, A. J., & Makela, J. J. (2019). Thermospheric weather as observed by ground-based fpis and modeled by gitm. *Journal of Geophysical Research: Space Physics*, *124*, 1307-1316. doi: 10.1029/2018JA026032
Hardy, D. A., Gussenhoven, M. S., & Holeman, E. (1985). A statistical model of auroral electron precipitation. *Journal of Geophysical Research*, *90* (A5), 4229-4248. doi: 10.1029/JA090iA05p04229
Heelis, R. A., & Coley, W. R. (1988). Global and local joule heating effects seen by de 2. *Journal of Geophysical Research*, *93* (A7), 7551-7557. doi: 10.1029/JA093iA07p07551
Heelis, R. A., Lowell, J. K., & Spiro, R. W. (1982). A model of the high-latitude ionospheric

convection pattern. *Journal of Geophysical Research*, *87*, 6339-6345. doi: 10.1029/JA087iA08p06339

Heinselman, C. J., & Nicolls, M. J. (2008). A bayesian approach to electric field and e-region neutral wind estimation with the poker flat advanced modular incoherent scatter radar. *Radio Science*, *43*. doi: 10.1029/2007RS003805

Heppner, J. P., & Maynard, N. C. (1987). Empirical high latitude electric field models. *Journal of Geophysical Research*, *92*, 4467-4489. doi: 10.1029/JA092iA05p04467

Iijima, T., & Potemra, T. A. (1976). Field-aligned currents in the dayside cusp observed by triad. *Journal of Geophysical Research*, *81* (34), 5971-5979. doi: 10.1029/JA081i034p05971

Janhunen, P., Koskinen, K. E. J., & Pulkinen, T. I. (1996, May). *A new global ionosphere-magnetosphere coupling simulation utilizing locally varying time step* (No. 205). Paris: European Space Agency.

Jones, E., Oliphant, R., Peterson, P., et al. (2001). *Scipy: Open source scientific tools for python.* Retrieved 2019-08-22, from http://www.scipy.org/

Kataoka, R., Fukunishi, H., Fujita, S., Tanaka, T., & Itonaga, M. (2004). Transient response of the earth's magnetosphere to a localized density pulse in the solar wind: Simulation of traveling convection vortices. *Journal of Geophysical Research*. doi: 10.1029/2003JA010287

Khazanov, G. V., Sibeck, D. G., & Zesta, E. (2017). Major pathways to electron distribution function formation in regions of diffuse aurora. *Journal of Geophysical Research: Space Physics*, *122*, 4251-4265. doi: 10.1002/2017JA023956

Knight, S. (1973). Parallel electric fields. *Planetary and Space Science*, *21* (5), 741-750. doi: 10.1016/0032-0633(73)90093-7

Knipp, D. J., Hapgood, M. A., & Welling, D. T. (2018). Communicating uncertainty and reliability in space weather data, models and applications. *Space Weather*, *16*, 1453-1454. doi: 10.1029/2018SW002083

Knipp, D. J., Tobiska, W. K., & Emery, B. A. (2004). Direct and indirect thermospheric heating sources for solar cycles 21–23. *Solar Physics*, *224* (495). doi: 10.1007/s11207-005-6393-4

Knipp, D. J., Welliver, T., McHard, M. G., Chun, F. K., Tobiska, W. K., & and, D. E. (2005). Climatology of extreme upper atmospheric heating events. *Advances in Space Research*, *36* (12), 2506-2510. doi: 10.1016/j.asr.2004.02.019

Lei, J., Liu, L., Wan, W., & Zhang, S.-R. (2004). Modeling the behavior of ionosphere above millstone hill during the september 21–27, 1998 storm. *Journal of Atmospheric and Solar-Terrestrial Physics*, *66* (12), 1093-1102. doi: 10.1016/j.jastp.2004.04.004

Liuzzo, L. R., Ridley, A. J., Perlongo, N. J., Mitchell, E. J., Conde, M., Hamption, D. L., . . . Nicolls, M. J. (2014). High-latitude ionospheric drivers and their effects on wind patterns in the thermosphere. *Journal of Geophysical Research: Space Physics*, *120*, 715-735. doi: 10.1002/2014JA020553

Lotko, W., & Zhang, B. (2018). Alfv´enic heating in the cusp ionosphere-thermosphere. *Journal of Geophysical Research: Space Physics*, *123*, 10368-10383. doi: 10.1029/2018JA025990

Lu, G., Hagan, M. E., Hausler, K., Doornbos, E., Bruinsma, S., Anderson, B. J., & Korth, H. (2014). Global ionospheric and thermospheric response to the 5 april 2010 geomagnetic storm: An integrated data-model investigation. *Journal of Geophysical Research: Space Physics*, *119*, 10358-10375. doi: 10.1002/2014JA020555

Lu, G., Richmond, A. D., Ruohoniemi, J. M., Greenwald, R. A., Hairston, M., Rich, F. J., & Evans, D. S. (2001). An investigation of the influence of data and model inputs on assimilative mapping of ionospheric electrodynamics. *Journal of Geophysical Research*, *106* (A1), 417-433. doi: 10.1029/2000JA000606

Matsuo, T., Richmond, A. D., & Hensel, K. (2003). High-latitude ionospheric electric field variability and electric potential derived from de-2 plasma drift measurements: Dependence on imf and dipole tilt. *Journal of Geophysical Research: Space Physics*, *108* (A1). doi: 10.1029/2002JA009429

Meng, X., Manucci, A. J., Verkhoglyadova, O. P., & Tsuratani, B. T. (2016). On forecasting ionospheric total electron content responses to high-speed solar wind streams. *Journal of Space Weather and Space Climate*, *6* (A19). doi: 10.1051/swsc/2016014
Mikhailov, A. V., & Foster, J. G. (1997). Daytime thermosphere above millstone hill during severe geomagnetic storms. *Journal of Geophysical Research*, *102*, 17275-17282. doi: 10.1029/97JA00879
Morley, S. K., Welling, D. T., & Woodroffe, J. R. (2018). Perturbed input ensemble modeling with the space weather modeling framework. *Space Weather*, *16*, 1330-1347. doi: 10.1029/2018SW002000
Newell, P. T., Sotirelis, T., Ruohoniemi, J. M., Carbary, J. F., Liou, K., Skura, J. P., . . . Rich, F. J. (2002). Ovation: Oval variation, assessment, tracking, intensity, and online nowcasting. *Annales Geophysicae*, *20*, 1039-1047. doi: 10.5194/angeo-20-1039-2002
Newell, P. T., Sotirelis, T., & Wing, S. (2009). Diffuse, monoenergetic, and broadband aurora: The global precipitation budget. *Journal of Geophysical Research*, *114*. doi: 10.1029/2009JA014326
Nicolls, M. J., Cosgrove, R., & Bahcivan, H. (2014). Estimating the vector electric field using monostatic, multibeam incoherent scatter radar measurements. *Radio Science*, *49*, 1124-1139. doi: 10.1002/2014RS005519
Nishimura, Y., Lyons, L., Zou, S., Angelopoulos, V., & Mende, S. (2010). Substorm triggering by new plasma intrusion: Themis all-sky imager observations. *Journal of Geophysical Research*, *115* (A07222). doi: 10.1029/2009JA015166
Ozturk, D. S., Zou, S., Ridley, A. J., & Slavin, J. A. (2018). Modeling study of the geospace system response to the solar wind dynamic pressure enhancement on 17 march 2015. *Journal of Geophysical Research: Space Physics*. doi: 10.1002/2017JA025099
Ozturk, D. S., Zou, S., Slavin, J. A., & Ridley, A. J. (2019). Response of the geospace system to the solar wind dynamic pressure decrease on 11 june 2017: Numerical models and observations. *Journal of Geophysical Research: Space Physics*, *124* (4), 2613-2627. doi: 10.1029/2018JA026315
Press, W. H., Teukolsky, S. A., Vetterling, W. T., & Flannery, B. P. (2007). *Numerical recipes: The art of scientific computing* (Third Edition ed.). Cambridge University Press.
Raeder, J., Berchem, J., & Ashour-Abdalla, M. (1998). The geospace environment modeling grand challenge: Results from a global geospace circulation model. *Journal of Geophysical Research: Space Physics*. doi: 10.1029/98JA00014
Rastatter, L., Shim, J. S., Kuznetsova, M. M., Kilcommons, L. M., Knipp, D. J., Codrescu, M., . . . Welling, D. (2016). Gem-cedar challenge: Poynting flux at dmsp and modeled joule heat. *Space Weather*, *14*, 113-135. doi: 10.1002/2015SW001238
Richards, P. G., Meier, R. R., & Wilkinson, P. J. (2010). On the consistency of satellite measurements of thermospheric composition and solar euv irradiance with australian ionosonde electron density data. *Journal of Geophysical Research*, *115*. doi: 10.1029/2010JA015368
Richmond, A. D. (2010). On the ionospheric application of poynting's theorem. *Journal of Geophysical Research*, *115* (A10311). doi: 10.1029/2010JA015768
Richmond, A. D., & Kamide, Y. (1988). Mapping electrodynamic features of the high-latitude ionosphere from localized observations: Technique. *Journal of Geophysical Research*, *93* (A6), 5741-5759. doi: 10.1029/JA093iA06p05741
Richmond, A. D., Lu, G., Emery, B. A., & Knipp, D. J. (1998). The amie procedure: Prospects for space weather specification and prediction. *Advances in Space Research*, *22*, 103-112. doi: 10.1016/S0273-1177(97)01108-3
Ridley, A. J., Deng, Y., & Toth, G. (2006). The global ionosphere-thermosphere model. *Journal of Atmospheric and Solar-Terrestrial Physics*. doi: 10.1016/j.jastp.2006.01.008
Ridley, A. J., Gombosi, T. I., & DeZeeuw, D. L. (2004). Ionospheric control of the magnetosphere: conductance. *Annales Geophysicae*, *22* (2), 567-584. doi: 10.5194/angeo-22-567-2004

Robinson, R. M., Vondrak, R. R., Miller, K., Dabbs, T., & Hardy, D. A. (1987). On calculating ionospheric conductances from the flux and energy of precipitating electrons. *Journal of Geophysical Research*, *92* (A3), 2565-2569. doi: 10.1029/JA092iA03p02565

Roble, R. G., & Ridley, E. C. (1987). An auroral model for the ncar thermospheric general circulation model (tgcm). *Annales Geophysicae*, *5* , 3369-382.

Rodger, A. S., Well, G. D., Moffett, R. J., & Bailey, G. J. (2001). The variability of joule heating, and its effects on the ionosphere and thermosphere. *Annales Geophysicae*, *19* , 773-781. doi: 10.5194/angeo-19-773-2001

Schunk, R., & Nagy, A. (2009). *Ionospheres: Physics, plasma physics, and chemistry (cambridge atmospheric and space science series)*. Cambridge: Cambridge University Press. doi: 10.1017/CBO9780511635342

Semeter, J., Butler, T. W., Zettergren, M., Heinselman, C. J., & Nicolls, M. J. (2010). Composite imaging of auroral forms and convective flows during a substorm cycle. *Journal of Geophysical Research*, *115* . doi: 10.1029/2009JA014931

Semeter, J. L., & Kamalabadi, F. (2005). Determination of primary electron spectra from incoherent scatter radar measurements of the auroral e region. *Radio Science*, *40* (RS2006). doi: 10.1029/2004RS003042

Sivadas, N., Semeter, J. L., Nishimura, Y., & Kero, A. (2017). Simultaneous measurements of substorm-related electron energization in the ionosphere and the plasma sheet. *Journal of Geophysical Research: Space Physics*, *122* , 10528-10547. doi: 10.1002/2017JA023995

Sydorenko, D., Rankin, R., & Yau, A. W. (2015). Enhanced n2 and o2 densities inferred from eiscat observations of pc5 waves and associated electron precipitation. *Journal of Geophysical Research: Space Physics*, *121* , 549-566. doi: 10.1002/2015JA021508

Syrjäsuo, M. T., & Donovan, E. (2002). Analysis of auroral images: Detection and tracking. *Geophysica*, *38* (1-2), 3-14.

Thayer, J. P. (1998). Height-resolved joule heating rates in the high-latitude e region and the influence of neutral winds. *Journal of Geophysical Research*, *103* (A1), 471-487. doi: 10.11029/97JA02536

Thayer, J. P., & Semeter, J. (2004). The convergence of magnetospheric energy flux in the polar atmosphere. *Journal of Atmospheric and Solar-Terrestrial Physics*, *66* , 807-824. doi: 10.1016/j.jastp.2004.01.035

Thayer, J. P., Vickrey, J. F., Heelis, R. A., & Gary, J. B. (1995). Interpretation and modeling of high-latitude electromagnetic energy flux. *Journal of Geophysical Research*. doi: 10.1029/95JA01159

Turner, N. E., Cramer, W. D., Earles, S. K., & Emery, B. A. (2009). Geoefficiency and energy partitioning in cir-driven and cme-driven storms. *Journal of Atmospheric and Solar-Terrestrial Physics*, *71* (10-11), 1023-1031. doi: 10.1016/j.jastp.2009.02.005

Verkhoglyadova, O. P., Meng, X., Manucci, A. J., & McGranaghan, R. M. (2018). Semianalytical estimation of energy deposition in the ionosphere by monochromatic alfvén waves. *Journal of Geophysical Research: Space Physics*, *123* , 5210-5222. doi: 10.1029/2017JA025097

Verkhoglyadova, O. P., Meng, X., Manucci, A. J., Mlynczak, M. G., Hunt, L. A., & Lu, G. (2017). Ionosphere-thermosphere energy budgets for the icme storms of march 2013 and 2015 estimated with gitm and observational proxies. *Space Weather*, *15* . doi: 10.1002/2017SW001650

Weimer, D. R. (2005). Improved ionpsheric electrodynamic models and application to calculating joule heating rates. *Journal of Geophysical Research*, *110* . doi: 10.1029/2004JA010884

Williams, P. J. S., Crowley, G., Schlegel, J., Virdi, T. S., McCrea, I., Watking, G., . . . Rodger, A. S. (1988). The generation and propagation of atmospheric gravity waves observed during the worldwide atmospheric gravity-wave study (wags). *Journal of Atmospheric and Terrestrial Physics*, *50* (4-5), 323-338. doi: 10.1016/0021-9169(88)90018-9

Wiltberger, M., Elkington, S., Guild, T., Baker, D., & Lyon, J. (2005). Simulations of isolated and storm time substorms. In T. I. Pulkinen, N. A. Tsyganenko, & R. H. Friedel (Eds.), (Vol. In The Inner Magnetosphere: Physics and Modeling, p. 271-281). American Geophysical Union. doi: 10.1029/155GM29

Wiltberger, M., Weigel, R. S., Lotko, W., & Fedder, J. A. (2009). Modeling seasonal variations of auroral particle precipitation in a global-scale magnetosphere-ionosphere simulation. *Journal of Geophysical Research*, *114* (A01204). doi:10.1029/2008JA013108

Yigit, E., & Ridley, A. J. (2011). Role of variability in determining the vertical wind speeds and structure. *Journal of Geophysical Research*, *116* (A12305). doi: 10.1029/2011JA016714

Yu., Y., & Ridley, A. J. (2011). Understanding the response of the ionosphere-magnetosphere system to sudden solar wind density increases. *Journal of Geophysical Research*. doi: 10.1029/2010JA015871

Zhang, X. Y., Zong, Q. G., Wang, Y. F., Zhang, H., Xie, L., Fu, S. Y., . . . Pu, Z. Y. (2010). Ulf waves excited by negative/positive solar wind dynamic pressure impulses at geosynchronous orbit. *Journal of Computational Physics*. doi: 10.1029/2009JA015016

Zhang, Y., & Paxton, L. J. (2008). An empirical kp-dependent global auroral model based on timed/guvi fuv data. *Journal of Atmospheric and Solar-Terrestrial Physics*, *70* (8-9), 1231-1242. doi: 10.1016/j.jastp.2008.03.008

Zhu, J., Ridley, A. J., & Deng, Y. (2016). Simulating electron and ion temperature in a global ionosphere thermosphere model: Validation and modeling an idealized substorm. *Journal of Atmospheric and Solar-Terrestrial Physics*, *138-139*, 243-260. doi: 10.1016/j.jastp.2016.01.005

Zhu, Q., Deng, Y., Richmond, A., McGranaghan, R. M., & Maute, A. (2019). Impacts of multiscale facs on the ionosphere-thermosphere system: Gitm simulation. *Journal of Geophysical Research: Space Physics*, *124*, 3532-3542. doi: 10.1029/2018JA026082

Zou, Y., Nishimura, Y., Lyons, L., Conde, M., Varney, R., Angelopoulos, V., & Mende, S. (2018). Mesoscale f region neutral winds associated with quasi-steady and transient nightside auroral forms. *Journal of Geophysical Research: Space Physics*, *123*, 7968-7984. doi: doi:10.1029/2018JA025457